Graphene and Carbon Nanotube Based Optoelectronic Devices

Zur Erlangung des akademischen Grades eines

DOKTORS DER NATURWISSENSCHAFTEN

durch die Fakultät für Physik

des Karlsruher Instituts für Technologie

genehmigte

DISSERTATION

von

Dipl.-Ing. Michael Engel

aus Sömmerda

Tag der mündlichen Prüfung:	22.06.2012
Referent:	Prof. Dr. Hilbert von Löhneysen
Korreferent:	Prof. Dr. Martin Wegener
Betreuer:	Prof. Dr. Ralph Krupke

GRAPHENE AND CARBON NANOTUBE BASED OPTOELECTRONIC DEVICES

MICHAEL ENGEL

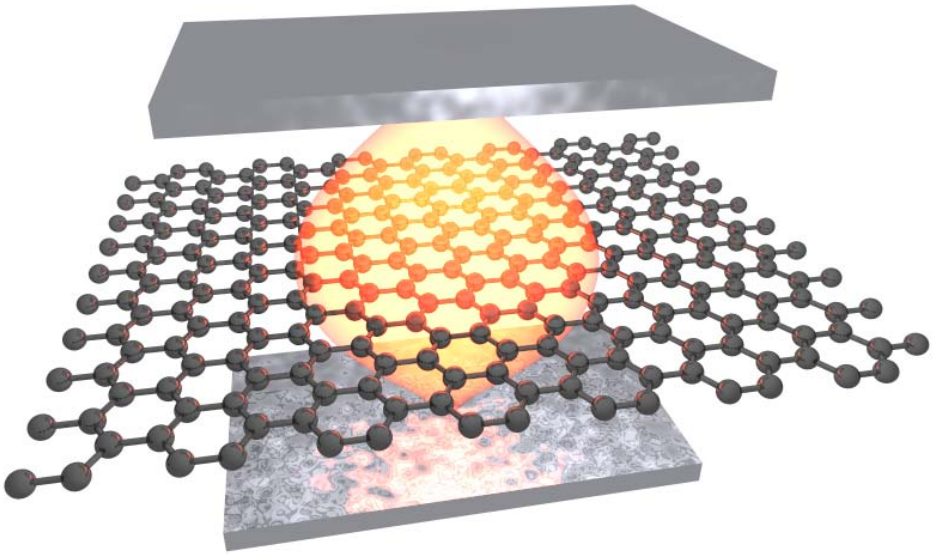

Physikalisches Institut
Fakultät für Physik
Karlsruher Institut für Technologie

June 2012

Michael Engel: *Graphene and Carbon Nanotube Based Optoelectronic Devices,*

SUPERVISORS:

Prof. Dr. Hilbert von Löhneysen

Prof. Dr. Martin Wegener

Prof. Dr. Ralph Krupke

LOCATION:

Karlsruhe

ABSTRACT

Scope of this work is to explore optoelectronic devices incorporating carbon nanotubes and graphene with the intention to both investigate fundamental physical processes of light generation and detection as well as to demonstrate proof-of-concept devices for optoelectronic applications.

In the first part of this thesis we report the monolithic integration of a graphene transistor with a planar optical microcavity. We find that both photocurrent generation as well as electrically excited thermal light emission of graphene can be controlled by the spectral properties of the microcavity. The device constitutes an implementation of a cavity-enhanced graphene light detector, as well as a demonstration of a fully integrated, narrow-band thermal light source. Most importantly, the optical confinement of graphene by the microcavity profoundly modifies the electrical transport characteristics of the integrated graphene transistor. The modifications of the electrical transport can be related to the microcavity-induced enhancement or inhibition of spontaneous emission of thermal photons. The concept of optical confinement of graphene enables a new class of functional devices as, for example, spectrally selective and highly directional light emitters, detectors, and modulators. Moreover, it opens up the opportunity for investigating fundamental, cavity-induced modifications of light-matter interactions in graphene.

In the second part of this thesis we perform laser-excited photocurrent microscopy for mapping the internal electrostatic potential profile of carbon nanotube (CNT) array devices with high spatial resolution. The measurements on optically transparent samples provide novel insights into the physical principles of device operation and

reveal performance-limiting local heterogeneities in the electrostatic potential profile that cannot be observed with the electron microscope. Most importantly, the experiments deliver photocurrent images from the underside of the CNT-metal contacts and enable the direct measurement of the charge carrier transfer length at the palladium-CNT interface and at the aluminum-CNT interface, respectively. We use the experimental results for deriving design rules for optimized layouts of CNT-based photovoltaic devices. Furthermore, we demonstrate full control of the electrostatic potential profile in CNT array devices that are equipped with local metal gates.

ZUSAMMENFASSUNG

Ziel dieser Arbeit ist optoelektronische Bauelemente auf Basis von Kohlenstoffnanoröhren und Graphen zu untersuchen. Die Intention ist sowohl zugrundeliegende physikalische Prozesse der Lichtgeneration und -detektion zu erforschen als auch ein proof-of-concept von Graphen-basierten optoelektronischen Baulementen für die Anwendung zu demonstrieren.

Im ersten Teil dieser Arbeit beschreiben wir den Prozess zur monolithischen Integration eines Graphen-Transistors in eine planare optische Mikrokavität. Wir beobachten, dass sowohl Photostromgeneration als auch elektrisch generierte thermische Lichtemission von Graphen mittels der spektralen Eigenschaften der Mikrokavität kontrolliert werden kann. Dieses Bauteil stellt die Implementierung eines kavitäten-verstärkten Graphen-Photodetektor sowie einer voll integrierten, schmalbandigen thermischen Lichtquelle dar. Im Besonderen modifiziert das veränderte Lichtfeld innerhalb der Kavität die elektrischen Transporteigenschaften des integrierten Graphen-Transistors massgeblich. Diese Modifikationen lassen sich auf die durch die Kavität bestimmte Unterdrückung bzw. Verstärkung der spontanen Emis-

sion zurückführen. Das Konzept eines veränderten Lichtfeldes innerhalb einer Mikrokavität in Kombination mit Graphen eröffnet eine völlig neue Klasse von funktionellen Bauteilen wie zum Beispiel spektral selektive und hoch gerichtete Lichtemitter, -detektoren und -modulatoren. Darüberhinaus eröffnet sich dadurch die Möglichkeit durch die Kavität bedingte Modifikationen der Wechselwirkung von Licht und Materie in Graphen zu untersuchen.

Im zweiten Teil dieser Arbeit stellen wir Ergebnisse zur laserinduzierten Photostrommikroskopie mit hoher räumlicher Auflösung an Bauteilen aus Arrays von Kohlenstoffnanoröhren vor. Diese Methode ermöglicht zudem die Abbildung der elektrostatischen Potentiallandschaft innerhalb eines Bauteils. Diese Messungen, durchgeführt an optisch tranparenten Proben, ermöglichen zudem neue Einblicke in die zugrundeliegenden physikalischen Prozesse und Wirkungsmechanismen. Desweiteren zeigen sich leistungslimitierende lokale Heterogenitäten in der elektrostatischen Potentiallandschaft, welche bei Inspektion mit einem Rasterelektronenmikroskop nicht zu erwarten sind. Darüberhinaus ermöglicht die Messmethodik den Photostrom auch unterhalb des Kontaktes am Interface zwischen Metall und Kohlenstoffnanoröhre zu messen, was eine direkte Messung der Ladungsträgertransferlänge zwischen Kontakten Kohlenstoffnanoröhre-Pd sowie Kohlenstoffnanoröhre-Al liefert. Zudem leiten wir aus den experimentellen Resultaten verbesserte Designs für optimierte Kohlenstoffnanoröhren-basierte photovoltaische Baulemenete ab. Abschließend demonstrieren wir volle Kontrolle des elektrostatischen Potentials innerhalb eines Kohlenstoffnanoröhrenarray Bauteils mittels lokaler Steuerelektroden.

PUBLICATIONS

The following represents a list of results that have been published in the course of this PhD thesis and before:

[1] M. Engel, M. Steiner, R.S. Sundaram, A.A. Green, M.C Hersam, R. Krupke, and P. Avouris. Electrostatic potential in carbon nanotube array devices. *accepted at ACS Nano*, 2012.

[2] M. Steiner, M. Engel, Y.-M. Lin, Y. Wu, K. Jenkins, D.B. Farmer, N. Yoder, A.A. Green, T.J. Seo, M.C Hersam, R. Krupke, and P. Avouris. High-frequency performance of scaled carbon nanotube array field-effect transistors. *accepted at Applied Physics Letters*, 2012.

[3] N. Rauhut, M. Engel, M. Steiner, R. Krupke, P. Avouris, and A. Hartschuh. Antenna-enhanced photocurrent microscopy on single-walled carbon nanotubes at 30 nm resolution. *ACS Nano*, 0(0):null, 0.

[4] M. Engel, M. Steiner, A. Lombardo, A.C. Ferrari, H.v. Löhneysen, P. Avouris, and R. Krupke. Light-matter interaction in a microcavity-controlled graphene transistor. *Nature Communications*, 3(906), 2012.

[5] C. Thiele, M. Engel, F. Hennrich, M.M. Kappes, K.-P. Johnsen, C.G. Frase, H.v. Löhneysen, and R. Krupke. Controlled fabrication of single-walled carbon nanotube electrodes by electron-beam-induced oxidation. *Applied Physics Letters*, 99(17):173105, 2011.

[6] M.H.P. Pfeiffer, N. Stürzl, C.W. Marquardt, M. Engel, S. Dehm, F. Hennrich, M.M. Kappes, U. Lemmer, and R. Krupke. Electro-

luminescence from chirality-sorted (9,7)-semiconducting carbon nanotube devices. *Optics Express*, 19(S6):A1184–A1189, 2011.

[7] R.S. Sundaram, M. Steiner, H.-Y. Chiu, M. Engel, A.A. Bol, R. Krupke, M. Burghard, K. Kern, and P. Avouris. The Graphene–Gold Interface and Its Implications for Nanoelectronics. *Nano Letters*, 11(9):3833–3837, 2011.

[8] M. Kinoshita, M. Steiner, M. Engel, J.P. Small, A.A. Green, M.C. Hersam, R. Krupke, E.E. Mendez, and P. Avouris. The polarized carbon nanotube thin film LED. *Optics Express*, 18(25):25738–25745, 2010.

[9] A. Vijayaraghavan, F. Hennrich, N. Stürzl, M. Engel, M. Ganzhorn, M. Oron-Carl, C.W. Marquardt, S. Dehm, S. Lebedkin, M.M. Kappes, and R. Krupke. Toward single-chirality carbon nanotube device arrays. *ACS Nano*, 4(5):2748–2754, 2010.

[10] M. Engel, J.P. Small, M. Steiner, Y.-M. Lin, A.A. Green, M.C. Hersam, and P. Avouris. Top-gated Thin Film FETs Fabricated from Arrays of Self-aligned Semiconducting Carbon Nanotubes. In *Device Research Conference, 2008*, pages 149–150, 2008.

[11] M. Engel, J.P. Small, M. Steiner, M. Freitag, A.A. Green, M.C. Hersam, and P. Avouris. Thin film nanotube transistors based on self-assembled, aligned, semiconducting carbon nanotube arrays. *ACS Nano*, 2(12):2445–2452, 2008.

[12] Michael Engel. Assessment of Carbon Nanotubes Separated by Electronic Type. Diploma Thesis, Technische Universität Ilmenau, Fakultät für Mathematik und Naturwissenschaften, 2008.

[13] C. Blank, S. Krischok, R. Gutt, M. Engel, J.A. Schaefer, J. Schawohl, L. Spiess, C. Knedlik, G. Ecke, F. Schrempel, E. Hueger, G. Hildebrand, and K. Liefeith. Ion implanted titanium surfaces for hard tissue replacement. *BIOmaterialien*, 8, 2007.

[14] S. Krischok, C. Blank, M. Engel, R. Gutt, G. Ecke, J. Schawohl, L. Spiess, F. Schrempel, G. Hildebrand, and K. Liefeith. Influence of ion implantation on titanium surfaces for medical applications. *Surface Science*, 601(18):3856–3860, 2007.

The theory of quantum electrodynamics describes Nature
as absurd from the point of view of common sense.
And it fully agrees with experiment.
So I hope you can accept Nature as She is - absurd.

— Richard P. Feynman [1]

ACKNOWLEDGMENTS

While there are many people that invaluably contributed to the work presented in this thesis, I would first like to thank Prof. Hilbert v. Löhneysen and Prof. Martin Wegener for acting as the referee and co-referee of this thesis, respectively. I am thankful for their time and patience in reading and evaluating the present work.

Foremost, I am very grateful to my supervisor Prof. Ralph Krupke for his support and giving me the freedom to explore ideas on my own. His constant encouragement and guidance during the years of my PhD is highly appreciated.

Results presented in this thesis would not have been possible without the close collaboration with the nanoscale science and technology group headed by Dr. Phaedon Avouris at the IBM T. J. Watson Research Center in Yorktown Heights, NY. In particular, I was very fortunate to have worked together with Dr. Mathias Steiner. I would like to thank him for his invaluable guidance and support during my PhD and the time spent at IBM where a large part of the results presented in this thesis have been obtained. Also, in the course of this study we were able to build a completely new experimental setup for optical, electrical, and optoelectronic characterization at the IBM T.J. Watson Research Center.

Success of an experiment is greatly determined by the quality of the samples and materials at hand. In that sense I was very lucky to

have worked together with some leading experts in there respective fields.

In case of the work involving graphene I am thankful to the group of Prof. Andrea C. Ferrari from the Electrical Engineering Division, Engineering Department, University of Cambridge and, in particular, to Dr. Antonio Lombardo for his expertise in preparation, transfer, and characterization of graphene samples. Supply of graphene samples, ever so slightly urgent, is highly appreciated.

In case of the work involving carbon nanotubes I am thankful to the group of Prof. Mark C. Hersam from the Department of Materials Science and Engineering and Department of Chemistry, Northwestern University and, in particular, to Dr. Alexander A. Green for supply of highly separated carbon nanotube material.

Further, I would like to acknowledge the important contributions made by Dr. Ravi S. Sundaram from the Max Planck Institute for Solid State Research, Stuttgart and by now at the Electrical Engineering Division, Engineering Department, University of Cambridge.

Also, I would like to thank the entire staff of the Institute of Nanotechnology at KIT and the nanoscale science and technology group at the IBM T. J. Watson Research Center who made the last years a pleasant and invaluable experience.

Financial support from the DFG - Center for Functional Nanostructures (CFN) within subproject B1.9 and a Research Travel Scholarship from the Karlsruhe House of Young Scientist (KHYS) is greatly acknowledged.

At last I am indebted to my family for their never ending support and encouragement over the last years without them I would not be where I am now.

CONTENTS

LIST OF FIGURES

1

INTRODUCTION

1.1 SCOPE OF THIS THESIS

The motivation of this thesis is to study novel optoelectronic devices based on graphene and carbon nanotubes coupled to photonic elements such as cavities or waveguides. One promise of graphene and carbon nanotubes is to eventually contribute to recent trends in optical on-chip and chip-to-chip communication. For that purpose true nanoscale light emitters, preferentially electrically driven, and detectors or, more generally electro-optic transducers are highly desirable. Early proof-of-concept experiments already showed the feasibility of this approach [2, 3, 4, 5, 6, 7]. We perform experiments along those lines to investigate the fundamental physical processes of light emission and detection in graphene and carbon nanotubes inside novel device geometries (see for example Fig. 1.1).

In the first part of this thesis we show the integration of graphene transistors into optical microcavities and study their light emission and detection properties as well as modification of the electrical transport in graphene due to the presence of the optical microcavity.

In the second part of this thesis our goal is to study photocurrent generation and electrostatic potentials spatially resolved in carbon nanotube array photodiodes employing different device designs.

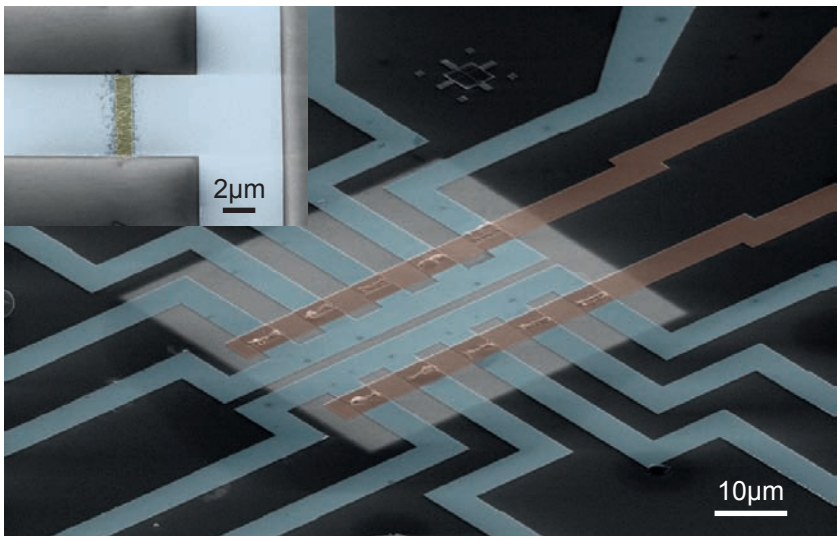

Figure 1.1: Example of cavity integrated carbon nanotube devices. The inset shows a carbon nanotube array device before deposition of cavity mirrors.

1.2 A SHORT SURVEY ON GRAPHENE AND CARBON NANOTUBES

In this section we will give a short overview on nano carbons, concentrating on carbon nanotubes and graphene. Carbon is a very special element within the periodic table of elements. It is very light, earth abundant, and all forms of life are made out of it. From a chemical point of view carbon is also very unique. It has four valence electrons that can form single, double, and triple bonds depending on the hybridization of its orbitals. Carbon's versatility to form all these different bonds is the reason why carbon occurs in such a diversity.

There is a variety of carbon allotropes known today, either naturally occurring or synthesized in the lab. These include materials like diamond, graphite, fullerenes, carbon nanotubes, exotic forms like londsdaleite, and the recently discovered [8, 9] or, better, rediscovered graphene [10, 11], i.e. single-layer graphite. Carbon can be found in column IV of the periodic table and its ground state electron configuration is $1s^2$, $2s^2$, $2p^2$. Thus, it has six electrons, two of them strongly bound in the $1s$ orbital and four of them more weakly bound occupying the $2s$ and $2p$ orbitals. The reason why carbon occurs in such

a variety of configurations can be explained by a concept known as hybridization, which has been introduced by Linus Carl Pauling [12] ([1]see Figure 1.2). Hybridization describes the phenomenon of atomic orbital mixing creating hybrid orbitals to lower the energy of the system. In the case of carbon this is feasible because of the small energy difference between the three $2p$ ($2p_x$,$2p_y$,$2p_z$) and the $2s$ orbital where the $2s$ orbital mixes with $2p$ electrons which is known as sp^i ($i = 1, 2, 3$) hybridization [13]. Carbon atoms in the lattice of graphene and carbon nanotubes are sp^2 hybridized. These three sp^2 hybrid orbitals are responsible for the rigidity of the covalent bonds between carbon atoms leaving one valence electron in the $2p_z$ orbital, which mainly determines the transport as well as the optical properties of graphene and carbon nanotubes.

Graphene, an atomic monolayer formed by carbon hexagons, is a material with extraordinary electrical and optical properties [14, 15, 16]. Consequently, there is a growing interest in graphene optoelectronics [17]. First demonstrations of graphene-based photodetectors [7], optical modulators [18], plasmonic devices [19, 20] and ultra-fast lasers [21] have been reported.

Carbon nanotubes are seamlessly rolled up hollow cylinders made of, as the name suggests, carbon atoms. Conceptionally, they can be envisioned as single-layer graphite, i.e. graphene, rolled up in a certain direction, which will be referred to as chirality. There are numerous ways this can be done leading to a huge heterogeneity of this peculiar material. Typically, carbon nanotubes have a length ranging from a few hundred nanometers up to centimeters [22] and diameters in the order of nanometers [23] resulting in a large aspect ratio of up to 10^7 [24].

Since their discovery in 1991 by Iijima [25] carbon nanotubes have sparked research efforts worldwide, which already led to promising results towards electronic [26], mechanical [27] and, for that matter,

1 Ball and stick illustration of atomic structures have been generated with the open-source molecular visualization program PyMOL `http://pymol.sourceforge.net/`.

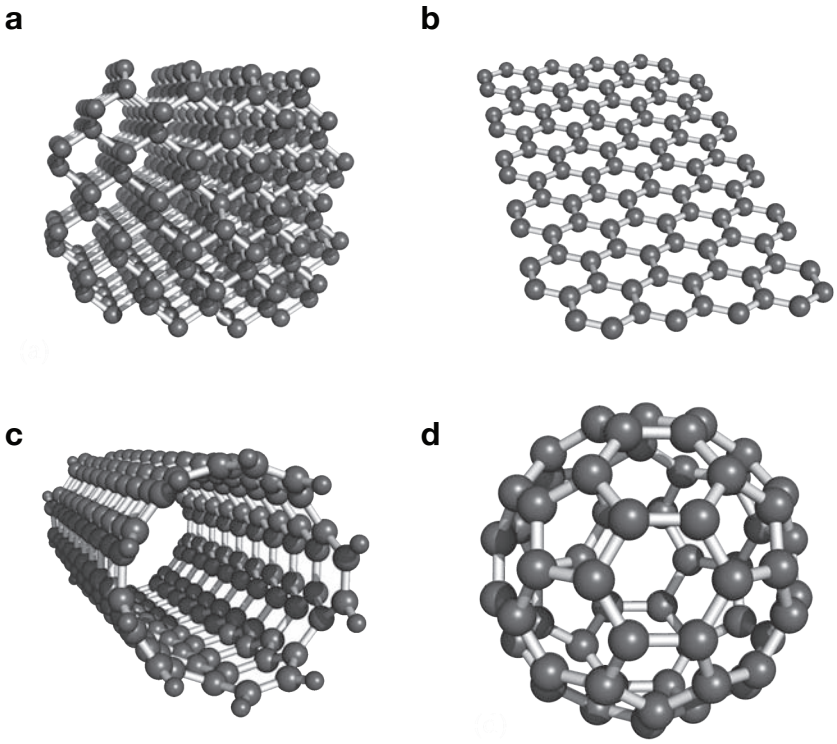

Figure 1.2: Gallery of all known carbon allotropes in order of decreasing dimensionality. (a) 3D diamond, (b) 2D single layer graphene or in its layered form known as graphite, (c) 1D, in this case, single-walled carbon nanotube, and (d) 0D C60 fullerene.

electromechanical [28, 29] applications. The first nanotubes found when viewed with a transmission electron microscope (TEM) had multiple shells and it was not until 1993 single-walled carbon nanotubes (SWNT), which are particularly interesting for electronics and optoelectronics, had been synthesized independently by Iijima [30] and Bethune [31]. Here we will focus on the promising optoelectronic properties of semiconducting carbon nanotubes[32].

2

THEORY

2.1 ELECTRONIC PROPERTIES OF GRAPHENE AND CARBON NANOTUBES

The electronic properties of graphene and carbon nanotubes and consequently their electrical transport properties are closely related as one can deduce within a single-particle tight-binding approach.

As a consequence of the sp^2 hybridization each carbon atom within the graphene lattice is bound to three neighboring carbon atoms, all in-plane, with a bond angle of 120°. Graphene has a hexagonal honeycomb-like lattice structure with unit vectors $\vec{a_1}$ and $\vec{a_2}$, which enclose an angle of 60° spanning the unit cell as shown in Fig. 2.1a. The unit cell has a diatomic basis comprising two equivalent carbon atoms A and B at $1/3(\vec{a_1} + \vec{a_2})$ and $2/3(\vec{a_1} + \vec{a_2})$ respectively.

Starting from the unit vectors $\vec{a_1}$ and $\vec{a_2}$ the reciprocal lattice vectors $\vec{b_1}$ and $\vec{b_2}$ are derived from the known relationships [33]. From that the first Brillouin zone of graphene is readily constructed (see Fig. 2.1b).

Based on the particular lattice structure the energy dispersion within the tight-binding approximation considering only nearest neighbor interactions reads as [34],

$$E(k_x, k_y)_{\mp} = \epsilon_{2p} \mp \gamma_0 \sqrt{1 + 4\cos\left(\frac{\sqrt{3}a_0 k_y}{2}\right)\cos\left(\frac{a_0 k_x}{2}\right) + 4\cos^2\left(\frac{a_0 k_x}{2}\right)}$$

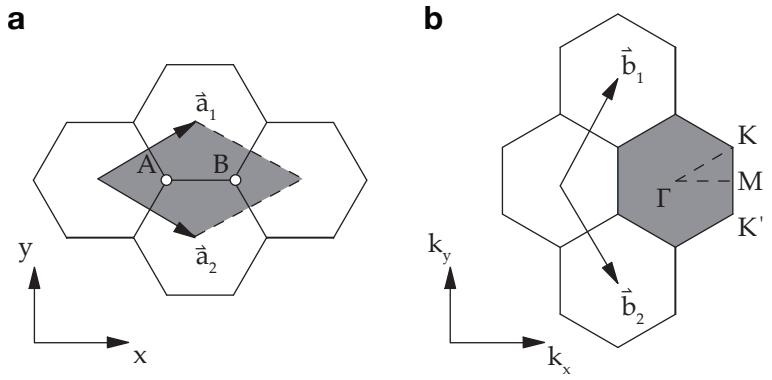

Figure 2.1: (a) Graphene unit cell in real space spanned by the unit vectors $\vec{a_1}$ and $\vec{a_2}$ with a diatomic basis consisting of two carbon atoms at points A and B. (b) Reciprocal lattice vectors $\vec{b_1}$ and $\vec{b_2}$ and the first Brillouin zone with the high symmetry points Γ, K and K′.

(2.1)

where the minus sign denotes the anti-bonding states of the conduction band and the plus sign the bonding states of the valence band. The tight-binding parameter γ_0 is defined negatively. Equation 2.1 contains two empirical parameters ϵ_{2p} and γ_0. Therefore, this result has to be calibrated against experimental data or more sophisticated theoretical approaches such as ab-initio techniques. This yields values around 0eV for ϵ_{2p} and $-3 \ldots -2.5$eV for γ_0, while different values are found in the literature. Reich et al. [34] nicely compared tight-binding calculations including up to the third-nearest neighbor interaction with ab-initio calculations. They found ab-initio and nearest-neighbor tight-binding calculations are only in good agreement in the vicinity of the K, K′ points.

In figure 2.2 the electronic band structure of graphene as first derived by Wallace [35] is plotted. As can be seen the conduction and valence bands touch at the K, K′ points, thus graphene is a semiconductor with zero band gap. Close to the K and K′ points the energy dispersion is approximately linear for low energy excitations.

In the case of carbon nanotubes there are additional boundary conditions that need to be fulfilled. While the $\vec{k}$-vector along the nanotube

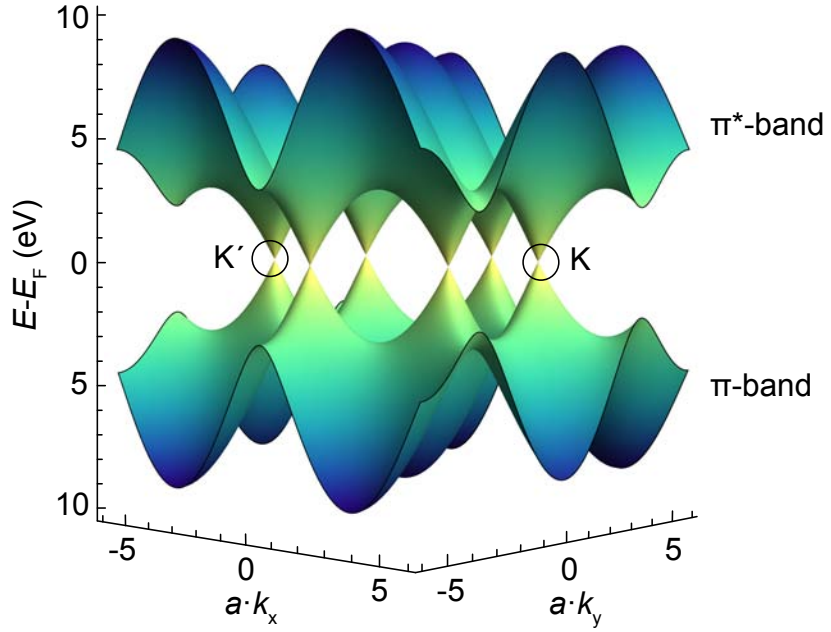

Figure 2.2: Electronic band structure of graphene. Conduction and valence band touch at six distinct points at the Fermi energy E_F. The false color scale represents the energy values of the energy bands as it is used in Fig. 2.3.

axis $\vec{k}_{\parallel}$ is continuous assuming that the nanotube is infinitely long, the $\vec{k}$-vector perpendicular to the nanotube axis $\vec{k}_{\perp}$ is quantized. This is due to the single-valued nature of the wave function, i.e. when going around the circumference an electron or phonon wave function, it has to accumulate a phase of integer multiples of 2π. As a consequence of this confinement sub bands emerge within the so called zone-folding approximation. The position of these sub bands depend on the chirality (n, m) of a carbon nanotube, i.e. the linear combination of unit vectors along the nanotube's circumference $(n \cdot \vec{a}_1 + m \cdot \vec{a}_2)$. In Fig. 2.3 two examples of allowed $\vec{k}$-values within the first Brillouin zone are shown.

Carbon nanotubes exhibit metallic or semiconducting behavior depending on the chiral indices (n, m) of the nanotube, i.e. whether electronic states at the K and K′ are allowed states. This condition is fulfilled for $3i = (m - n)$ where i is an integer [36]. Note that the phonon band structure is also quantized in analogy to the electronic

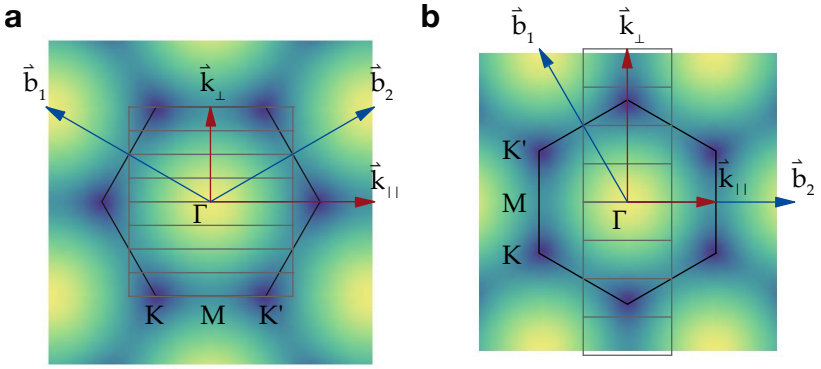

Figure 2.3: First Brillouin zone of a (a) (4,4) and (b) a (4,0) carbon nanotube showing the quantization of allowed states along $\vec{k}_\perp$ and the continuity of states along $\vec{k}_{||}$ in $\vec{k}$-space. The background shows a contour plot of the electronic band structure of graphene.

band structure shown experimentally by Hone et al. [37]. The electronic band structure[1] for two carbon nanotubes is plotted in Fig. 2.4.

From the electronic band structure we can derive information regarding the transport properties of graphene and semiconducting carbon nanotubes as they will be of importance in chapter 4 and 5 respectively. In the case of graphene in a field-effect transistor (FET) geometry the conductivity can be tuned continuously by a gate electrode from hole valence band to electron conduction. There is a minimum in the conductivity at the so called Dirac or charge neutrality point, i.e. the touching point of valence and conduction band [8]. In contrast semiconducting carbon nanotubes within a FET geometry exhibit a clear off-state, or transport gap, when sweeping the gate voltage [39, 40].

1 Band structures have been calculated using CNTbands 2.0 [38] on `http://www.nanohub.org` within the tight-binding approximation.

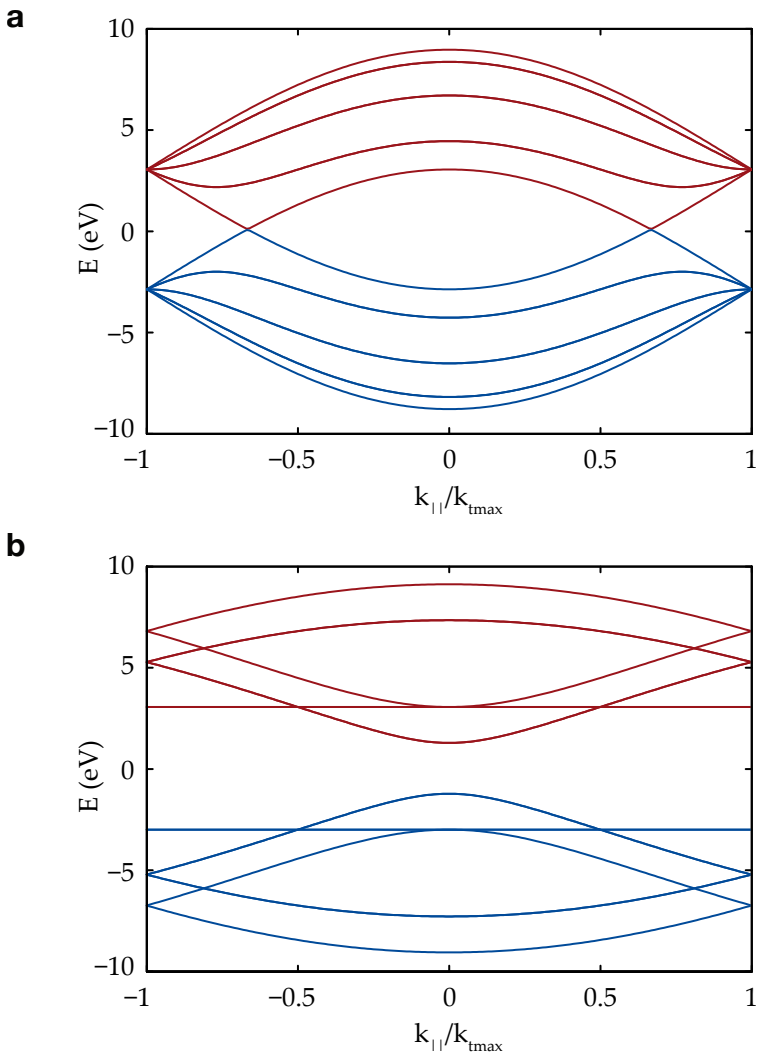

Figure 2.4: Band structure of a (a) (4,4) and (b) (4,0) carbon nanotube. Conduction and valence subbands are colored red and blue respectively.

2.2 OPTICAL PROPERTIES OF GRAPHENE AND CARBON NANOTUBES

In general the optical properties of graphene are governed by its dynamical conductivity $\sigma(\omega)$. For frequencies greater than the typical

inverse scattering time $\omega \gg \tau^{-1}$ the optical conductivity $\sigma(\omega)$ within a single-particle tight-binding theory can be written as [41, 42]

$$\sigma(\omega) = \frac{ie^2\omega}{\pi\hbar}\left[\int_{-\infty}^{+\infty} d\epsilon \frac{|\epsilon|}{\omega^2}\frac{df_0(\epsilon)}{d\epsilon} - \int_0^{+\infty} d\epsilon \frac{f_0(-\epsilon) - f_0(\epsilon)}{(\hbar\omega + i\delta)^2 - 4\epsilon^2}\right] \quad (2.2)$$

where $f_0 = (\exp[(\epsilon - \mu)/k_BT] + 1)^{-1}$ is the Fermi function, μ is the chemical potential, k_B is Boltzmann's constant, and T is the temperature. The first integration in Eq. 2.2 gives the contribution from intraband processes, which after integration reads as

$$\sigma^{intra}(\omega) = \frac{2ie^2k_BT}{\pi\hbar(\omega + i\tau^{-1})}\ln[2\cosh(\mu/2k_BT)] \quad (2.3)$$

which for temperatures $k_BT \ll \mu$ reduces to

$$\sigma^{intra}(\omega) = \frac{ie^2|\mu|}{\pi\hbar^2(\omega + i\tau^{-1})} \quad (2.4)$$

The second term in equation 2.2 describes the contribution to the conductivity from interband processes. This is the part we are most interested in and is the dominating contribution for the experiments we will present in chapter 4. After integration of the second term we arrive at

$$\sigma^{inter}(\omega) = \frac{e^2}{4\hbar}\left[\theta(\hbar\omega - 2\mu) - \frac{i}{2\pi}\ln\frac{(\hbar\omega + 2\mu)^2}{(\omega - 2\mu)^2}\right] \quad (2.5)$$

where $\theta(\hbar\omega - 2\mu)$ is the step function. We can see that for transition frequencies $\hbar\omega \gg \mu$ the expression for σ^{inter} reduces to

$$\sigma^{inter}(\omega) = \frac{e^2}{4\hbar}. \quad (2.6)$$

This result has important implications for the optical properties of graphene. Since σ^{inter} is constant, optical properties such as the

transmission T and absorption A should also be constant according to

$$A = (1 - T) = \frac{4\pi}{c}\sigma = \pi\alpha = 2.3\% \tag{2.7}$$

The relationship $A = 1 - T$ holds because the reflectance R is negligible ($R = 1/4\pi^2\alpha^2 T < 0.1\%$). Experimental verification of this theoretical prediction has been given by Nair et al. [43] Figure 2.5 shows the results obtained by Nair et al.. For light transmission throughout the visible, graphene indeed only absorbs 2.3% of impinging light. Further, absorption as a function of graphene layers is additive which points towards a negligible interlayer coupling with respect to the optical properties of graphene. In chapter 4 we will show how we can alter this constant broadband response by coupling graphene to an optical microcavity.

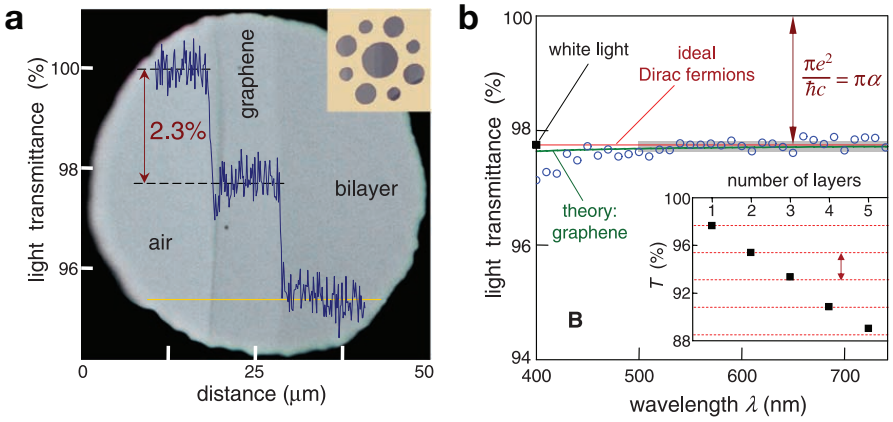

Figure 2.5: Universal transmission of graphene. (a) Experimental setup for measuring the optical transmission of graphene; micromechanical exfoliation of graphene on a copper grids with apertures of varying size. (b) Constant transmission through a freely suspended graphene layer over visible wavelength range. The inset shows transmission values as a function of the number of graphene layers. Images are taken from [43]

Next we discuss the optical properties of carbon nanotubes. As with the electronic properties, the additional boundary conditions

that lead to a one-dimensional confinement have profound effects on the optical properties of CNTs. The confinement along the circumference of a CNT gives rise to sharp singularities, so-called van Hove singularities, in the density of states[2] of CNTs [23](see Fig. 2.6). This single-particle-based model with the addition of some scaling factors works well to explain experimental observations such as photoluminescence [44], but many-body effects are thought to be strong in systems with reduced dimensionality, in particular electron-hole interactions [45]. Calculations predict binding energies of strongly bound electron-pairs, i.e. excitons, in carbon nanotubes to be of the order of $\sim$ 1eV [46]. The prediction that indeed the optical resonances arise from excitons were confirmed independently by two groups in 2005 [47, 48].

2.3 SPONTANEOUS EMISSION / ABSORPTION IN OPTICAL MICROCAVITIES

In the following we want to shortly discuss how we can change the rate of spontaneous emission/absorption by an optical microcavity. As an instructive example we envision placing a two-level system inside a planar microcavity. The Hamiltonian of the two-level system is described as

$$H_A = \hbar\omega_e |e\rangle\langle e| + \hbar\omega_g |g\rangle\langle g| \tag{2.8}$$

where $|e\rangle$ is the excited state, $|g\rangle$ is the ground state, $\hbar\omega_e$ and $\hbar\omega_g$ are the respective energies.

The quantized electromagnetic field is written as,

$$H_F = \sum_i^{\infty} \hbar\omega_i \left(a_i^\dagger a_i + 1/2\right) \tag{2.9}$$

2 Density of states have been calculated using CNTbands 2.0 [38] on `http://www.nanohub.org` within the tight-binding approximation.

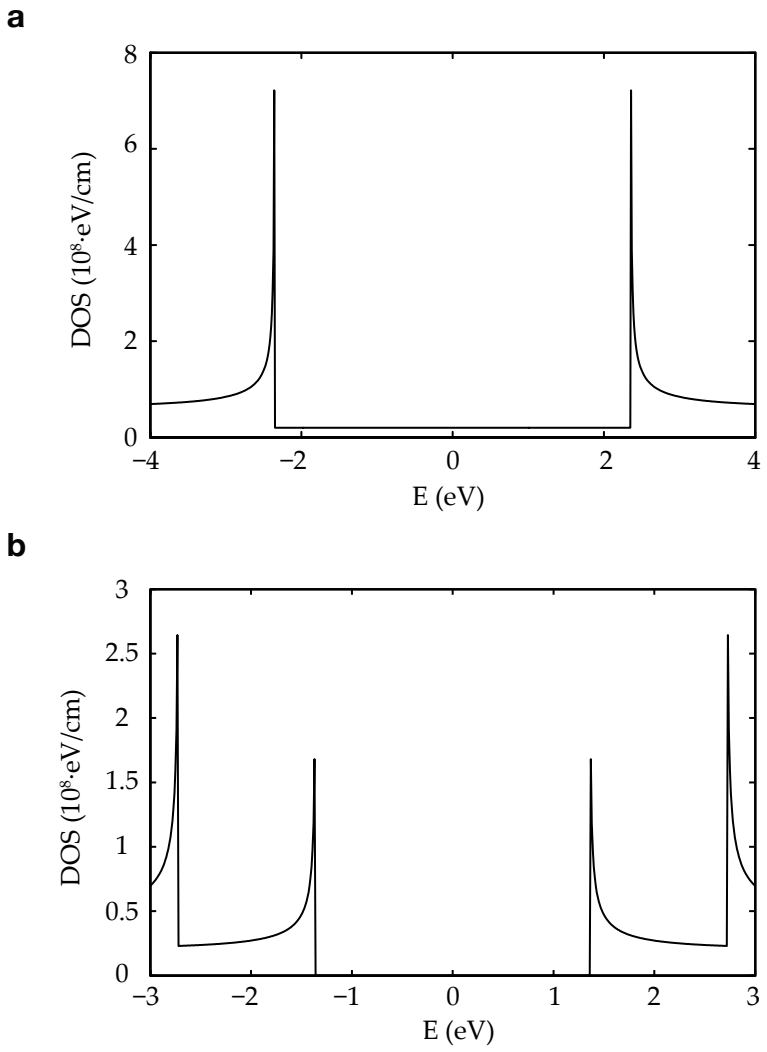

Figure 2.6: Corresponding density of states of a (a) (4,4) and (b) (4,0) carbon nanotube for the band structures shown in Fig. 2.4.

where $a^\dagger$ and a is the creation and annihilation operator and $\hbar\omega_i$ is the associated energy of the field mode.

A two-level system, e.g. an atom or molecule, in the excited state would remain excited forever unless it couples to its environment via for example the dipole coupling to a single electromagnetic field mode of frequency $\hbar\omega_i$. The interaction between between a single

two-level system and modes of the electromagnetic field in the dipole approximation can be written as

$$H_{int} = -\vec{d} \cdot \vec{E} \tag{2.10}$$

where $\vec{d}$ is the electric dipole moment and $\vec{E}$ is the electric field. The total Hamiltonian then reads

$$H = H_A + H_F + H_{int}. \tag{2.11}$$

Now the rate of spontaneous emission Γ or the excited-state inverse lifetime τ^{-1} (see Fig. 2.7a) is typically calculated using Fermi's golden rule [49] which yields

$$\Gamma = \tau^{-1} = \frac{2\pi}{\hbar^2} \int |\langle e|H_{int}|g\rangle|^2 \rho(\omega)\mathcal{L}(\omega)d\omega. \tag{2.12}$$

Here $\langle e|H_{int}|g\rangle$ is the dipole matrix element, $\rho(\omega)$ is the photonic mode density, and $\mathcal{L}(\omega)$ is the final state distribution that suffices

$$\int L(\omega)d\omega = 1. \tag{2.13}$$

From this we can identify three possibilities to change the rate of spontaneous emission by either the coupling strength between emitter and the electromagnetic field, by the photonic mode density, or the final state distribution.

In this work we accomplish a rate alteration by changing the photonic mode density. By placing an emitter in a planar microcavity enclosed by metallic mirrors we change the density of allowed states such that radiative recombination into the ground state is enhanced for transitions $\omega_i = \omega_e - \omega_g$.

In terms of cavity mirror spacing L this is expressed as $L = n\lambda/2$ where n is an integer (see Fig. 2.7b). Conversely if $L \neq n\lambda/2$ spontaneous emission is inhibited (see Fig. 2.7c). Historically it was believed

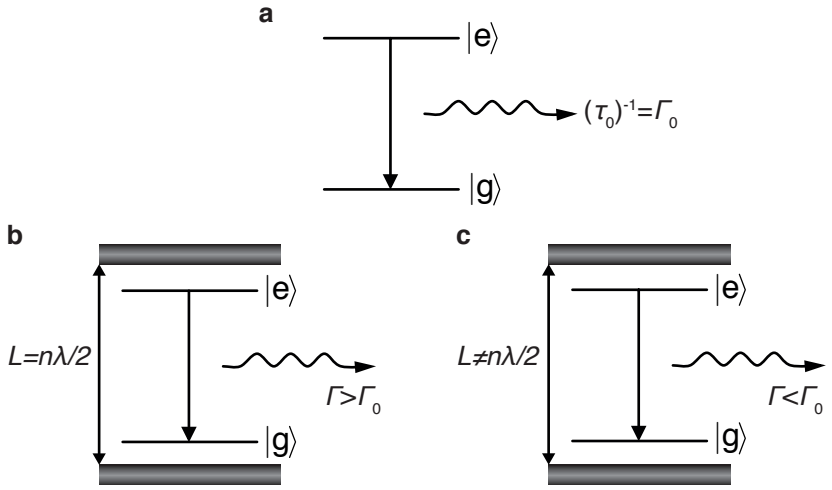

Figure 2.7: Schematic illustration of the rate change of spontaneous emission in non-confined, free space (a) when imposing boundary conditions by placing an emitter inside a planar cavity with mirror spacing L. The rate of spontaneous emission increases when the mirror spacing L is a multiple of $\lambda/2$ (b) or decreases when $L \neq n\lambda/2$ (c), compared to the non-confined case.

that Γ or τ^{-1} is an intrinsic property of an emitter in contrast to the arguments outlined so far. The first one to demonstrate that Γ indeed is a function of the emitter's coupling to its environment was Purcell in 1946 [50]. The degree of enhanced spontaneous emission is expressed as the ratio of free space to cavity photonic mode density known as the Purcell enhancement factor,

$$P = \frac{3}{4\pi^2}\left(\frac{\lambda}{n}\right)^3 \frac{Q}{V} \tag{2.14}$$

where λ is the wavelength, Q is the cavity quality factor, and V is the mode volume. From Eq. 2.14 we can see that to maximize the rate of spontaneous emission for a given wavelength λ we want to maximize the cavity quality factor Q and minimize the mode volume V. The minimum achievable mode volume is at the lowest-order resonance $n = 1$ for $L = \lambda/2$.

3

EXPERIMENTAL

In the following we describe the experimental setup the measurements presented in chapter 4 and 5 have been carried out with. The setup has been built around a customized inverted optical microscope[1]. The microscope is equipped with a 3-axis nanopositioning stage P562.3CD operated by a controller unit E509.C34 (both Physik Instrumente PI GmbH & Co. KG) that allows for scanning the sample with respect to an optical probe. Emphasis has been put on a compact design to ensure mechanical stability particularly crucial for long-time scans. For optical excitation we can couple in a variety of light sources, depending on the experimental requirements, into the back aperture of an objective lens.

For example the photocurrent spectroscopy in 4.2.3 has been performed with a CW dye laser and the photocurrent studies presented in chapter 5 have been carried out with an He-Ne gas laser ($\lambda = 632.8$nm) and an argon-ion laser ($\lambda = 514.5$nm). In the following, an overview on the various light sources and detection systems is given.

LIGHT SOURCES

1. He-Ne gas laser model 1144P (JDS Uniphase Corporation)

1 The setup described has been built at the IBM T.J. Watson Research Center together with Dr. Mathias Steiner and expert technical assistance from the mechanical workshop of the Central Scientific Services (CSS) at IBM.

2. Argon-ion laser Innova Sabre (Coherent, Inc.)

3. CR-599 dye laser (Coherent, Inc.), operated with Rhodamine 590 chloride (Exciton) dissolved in ethylene glycol.

4. White light sources

   A Fiber coupled tungsten light source L10671 (Hamamatsu Photonics K.K.)

   B Fiber-optic illuminator "Fiber-Lite" model 190 (Dolan-Jenner Industries, Inc.)

DETECTION SYSTEM 1 (VIS/NIR)

A monochromator HR550 (HORIBA Instruments Inc.) equipped with 3 different gratings (1200gr./mm $\lambda_{blaze} = 630$nm, 300gr./mm $\lambda_{blaze} = 600$nm, 150gr./mm $\lambda_{blaze} = 1200$nm). The dispersed light is detected with either a CCD array (1024x256-BIDD-1LS (LN-cooled), Symphony controller (HORIBA Instruments Inc.)) with increased sensitivity in the NIR region or an InGaAs array (IGA1024x1-25-1700-1LS (LN-cooled), Symphony controller (HORIBA Instruments Inc.)) that covers the wavelength range beyond the visible from 800nm to 1700nm.

DETECTION SYSTEM 2 (UV/VIS)

A monochromator Triax 190 (HORIBA Instruments Inc.) equipped with 3 different gratings (1200gr./mm $\lambda_{blaze} = 500$nm, 600gr./mm $\lambda_{blaze} = 1000$nm, 150gr./mm $\lambda_{blaze} = 500$nm). The dispersed light is detected with a CCD array (2000x800-9 (LN-cooled), Symphony controller (HORIBA Instruments Inc.)) with increased sensitivity in the UV region.

DETECTION SYSTEM 3 (VIS)

Fast light detection over the visible wavelength range or a small part thereof is achieved with an avalanche photodiode PDM 50CT (Micro Photon Devices S.r.l.) in combination with a band pass filter to spectrally select a defined wavelength region.

ELECTRONIC EQUIPMENT

Devices are electrically addressed with coaxial probes (Micromanipulator 79-6000-R-03) using probe tips (Micromanipulator 7B) mounted to 3-axis micromanipulators (Newport M-MT-XYZ) attached to the raster scanning unit.

As DC current and voltage sources we use different source-measuring units (Keithley 6430, Keithley 2400, National Instruments NI USB-6229 BNC). Electrical signals are detected with an current preamplifier (DL instruments, Model 1211 Current Preamplifier) or voltage preamplifier (DL instruments, Model 1201 Voltage Preamplifier). Read-out of the preamplifiers is achieved by a digital multimeter (Keithley 2000) connected to a PC via GPIB. For experiments that require higher sensitivity we adopt a lock-in measuring scheme using a lock-in amplifier (SRS 830 DSP). All electrical inputs and outputs are controlled via GPIB with a PC using the meaSureit 3.6 software[2].

2 http://sites.google.com/site/measureitteam/

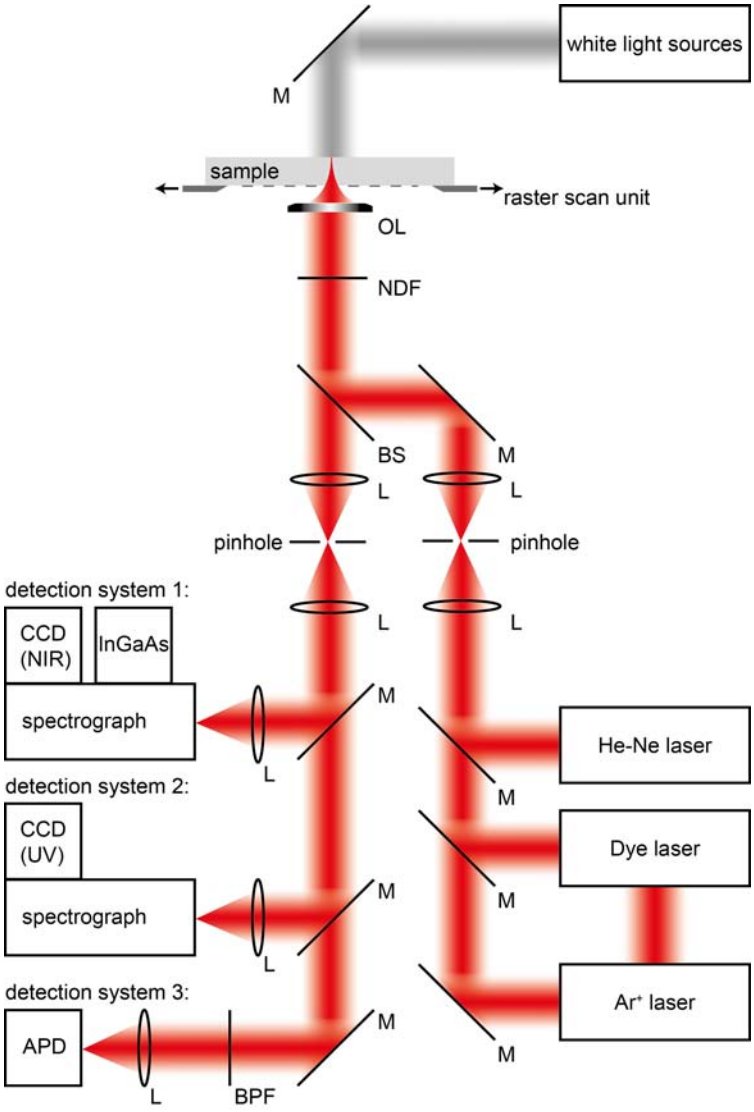

Figure 3.1: Schematic visualization of the optical part of the experimental setup showing the various excitation sources and detection systems (M: mirror, L: lens, OL: objective lens, BS: beam splitter, NDF: neutral density filter, BPF: band pass filter).

4

LIGHT-MATTER INTERACTION IN A MICROCAVITY-CONTROLLED GRAPHENE TRANSISTOR

Due to its two-dimensional nature, graphene is ideally suited for integration within a planar $\lambda/2$ microcavity. A planar microcavity is the basic photonic structure that confines optical fields between two highly reflecting mirrors with a spacing of only one half wavelength of light. The optical confinement could provide a feasible way of controlling the otherwise featureless optical absorption [43, 51] as well as the spectrally broad thermal emission [52, 53] of graphene.

According to Fermi's golden rule [54], the spontaneous photon emission/absorption rate is determined by the local photonic mode density that can be significantly altered inside an optical microcavity [55]. The cavity-induced confinement enables the enhancement [50] or the inhibition [56] of the light emission (absorption) rate of the intra-cavity medium. The in-plane transition dipole moment of the intra-cavity medium couples to the longitudinal cavity mode of the cavity with wavelength-dependent efficiency, and the coupling strength is maximized at the anti-node of the optical field located at the cavity center [57, 58]. Fig. 4.1 visualizes the principle of confining graphene by a planar optical cavity.

The cavity-induced rate enhancement, or Purcell effect, has already been demonstrated with quasi 2-D quantum wells, as well as quasi 1-D and 0-D systems such as atoms, molecules, quantum dots and other nanoparticles [55]. However, embedding a truly 2-D material like gra-

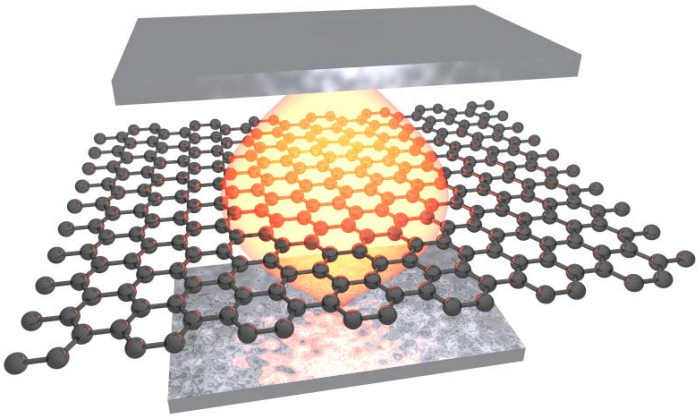

Figure 4.1: Visualization of a graphene layer located at the center of a planar optical $\lambda/2$ microcavity. The optical coupling is maximized if the graphene layer is oriented parallel to the cavity mirrors. The visualization of the optical field distribution of the fundamental cavity mode displays the $|E_{x,y}(z)|^2$ component.

phene into a planar cavity has not been reported so far, an approach yet highly desirable because of two main reasons. First, the coupling area, i.e. the spatial overlap between graphene and the cavity, can be extended to the micrometer scale within the two dimensions of the cavity plane, while preserving the optical confinement of graphene with respect to the cavity normal on the length scale of $\lambda/2$ (see Fig. 4.1). This is important because optical transitions in graphene are associated with in-plane transition dipole moments ($\pi - \pi^*$ transitions), thus rendering the 1D, planar cavity confinement, highly efficient. Second, the Fermi energy and density of states of graphene can be tuned easily by directly connecting it to electrodes, thus enabling charge carrier control, electrical transport, and heating within the active area of the cavity. Graphene hence opens a unique experimental approach towards cavity quantum electrodynamics on the nanometer scale with a current-carrying intra-cavity medium of atomic thickness.

To expand on this point there are two main reasons why the one-dimensional, planar cavity confinement is efficient in case of graphene. First, owing to the molecular structure of sp^2-carbon, the optical (electron and phonon) transitions in graphene are mainly associated with in-plane transition dipole moments [59]. This means that optical confinement in the two lateral dimensions is more efficient compared to, e.g., quantum dots with significant transition dipole moments in all three dimensions. Lateral emissions, i.e. parallel to the cavity mirrors, are hence expected to be weak. In Fig. 4.20 we provide experimental evidence that coupling to off-axis (higher order transversal) cavity modes for angles larger than 30 degrees with respect to the cavity normal is indeed insignificant. Coupling to lateral cavity modes is further suppressed in the specific configuration used for our experiments, due to the presence of the metal contacts forming boundaries for optical field propagation along the channel direction. Second, unlike distributed Bragg reflectors, metallic mirrors provide steady optical confinement conditions (no leaky off-axis modes) and maintain high optical reflectivities over a wide angular range and a broad spectral range (not just a narrow stop band). For the optical confinement of broadband emitters, this approach offers distinct advantages over dielectric mirrors, leading to a noticeable modulation of the experimental spontaneous emission (SpE) rate. Steiner et al. present in [58] consistent experimental and theoretical evidence of SpE rate modulations for a molecular broadband emitter enclosed within a $\lambda/2$-cavity. The optical confinement in their work is accomplished by silver mirrors made of 30nm, 60nm (the same as in the present case) which allows for a SpE enhancement of 2.5 and a SpE inhibition of 0.2 by directly monitoring the molecular excited states dynamics in the time domain. The latter work also provided a comprehensive experimental and theoretical analysis of the angular dependence of SpE rate modifications experienced by a broadband emitter in the planar metal mirror cavity, including the angular redistribution of the light emission.

As compared to dielectric mirrors having narrow-band on-axis reflectivity and leaky off-axis modes, metal mirrors support resonant coupling to off-axis cavity modes that contribute to the overall SpE rate enhancement. This is of particular importance in the case of broadband emitters that simultaneously couple to the all available on- and off-axis cavity modes. In return, metallic mirrors provide efficient boundary conditions for SpE-inhibition at off-resonant wavelengths and angles. In other words, metallic cavities do not provide the best possible spectral filtering, due to limited mirror reflectivities, but they provide good overall (on- and off-axis) optical confinement for enclosed broadband emitters. Based on Eq. (29) in Ref. [60]

$$r = \sqrt{\frac{\pi \lambda_{cavity} L (R_1 R_2)^{0.25}}{8n(1-\sqrt{R_1 R_2})}}, \tag{4.1}$$

we can estimate the spatial (lateral) mode diameter $2r$ of our planar microcavity, where λ_{cavity} is the cavity resonance wavelength, R_1 and R_2 are the mirror reflectivities, and n is an effective index of refraction of the intra-cavity medium. Taking into account the actual optical parameters ($R_1 = 0.9$, $R_2 = 0.7$, $n = 1.8$, $L = 155$nm) we determine $2r$ to be 0.8μm at an emission wavelength of 925nm. We have accounted for this in the design of our cavity by extending the lateral dimensions of the cavity mirrors well beyond the graphene layer (see Fig. 4.9b) to avoid incomplete optical confinement and direct coupling to free space of a substantial fraction of the emission. Also, in agreement with previous studies [61, 62] the coupling efficiency to plasmon modes of the metal mirrors is insignificant for emitter-mirror distances above 50nm.

4.1 SAMPLE FABRICATION

In figure 4.2 we outline the process flow showing the most important fabrication steps.

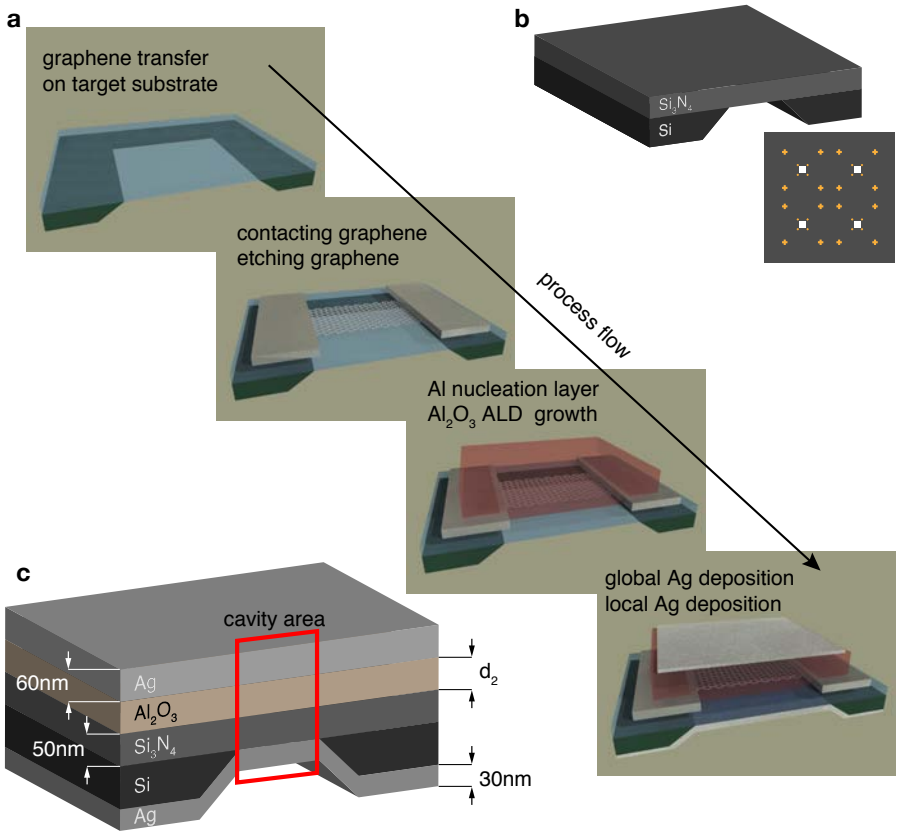

Figure 4.2: (a) Process flow showing the main steps of monolithic integration. (b) Schematic of the target substrate, a 50nm Si_3N_4 membrane with an area of $50x50\mu m^2$. Also shown is a top-view schematic with the predefined metallic markers defined by e-beam lithography used for orientation during the transfer process and re-alignment for later lithography steps. (c) Schematic of the multilayer stack with detailing the different materials and layer thickness. The red box highlights the microcavity.

Fabrication starts with preparation of graphene sheets via micromechanical cleavage of graphite on Si substrates covered with 300nm of SiO_2. Single layer graphene (SLG) is identified by a combination of optical microscopy and Raman spectroscopy. Three layers of 950K poly(methyl methacrylate) (PMMA) are then spin-coated on the substrates where flakes are deposited. The samples are subsequently immersed in de-ionized (DI) water at 90°C for 2 hours, resulting in the detachment of the polymer film, due to the intercalation of water at the polymer-SiO_2 interface. Graphene flakes stick to the PMMA film,

and can thus be removed from the original substrate[1]. The target substrate is a suspended Si_3N_4 layer [$n(Si_3N_4) \approx 2$] with a thickness of 50nm and area of $50x50\mu m^2$, supported by a Si frame having a thickness of 200μm. We defined metallic markers by e-beam lithography and e-beam evaporation of 5nm Ti and 50nm Au on the target substrate. These markers are used for orientation during the transfer process and re-alignment for all following e-beam lithography steps. The PMMA+graphene film is transferred onto the suspended Si_3N_4 layer. Because a thin layer of water is trapped at the substrate-polymer interface, the latter can be moved across the target substrate allowing accurate positioning of a chosen graphene flake onto a specific location on the Si_3N_4 membrane. The sample is then left to dry, and finally PMMA is dissolved by acetone drop-casting followed by immersion, resulting in the gentle release of the selected graphene flake on the target substrate. Success of the transfer is confirmed by Raman spectroscopy, which also proves the absence of process-induced structural defects. Fig. 4.3 shows an example of the transfer process.

Metallic contacts are fabricated by e-beam lithography and sequential deposition of 0.5nm Ti and 50nm Pd by e-beam evaporation. Pd is chosen as the contact material which has been shown to provide the highest transmission probability of charge carriers into the graphene channel [63].

In a next step, the selected SLGs are shaped by oxygen plasma etching into different sizes ($0.5x0.5\mu m^2$, $1x1\mu m^2$, $2x2\mu m^2$, and $4x4\mu m^2$)[2]. We then deposit a nucleation layer of 2nm Al on top of the SLGs to ensure homogeneous growth [64], followed by an Al_2O_3 layer [$n(Al_2O_3) \approx 1.7$] grown by atomic layer deposition of varying thickness.

The thickness of the intra-cavity dielectrics determines the resonance wavelength of the optical microcavity. In order to make the

1 Exfoliation, transfer, and accompanying Raman characterization of graphene flakes has been performed by Dr. Antonio Lombardo (Electrical Engineering Division, Engineering Department, University of Cambridge).

2 Preparation and characterization of samples has been carried at the IBM T.J. Watson Research Center unless stated otherwise.

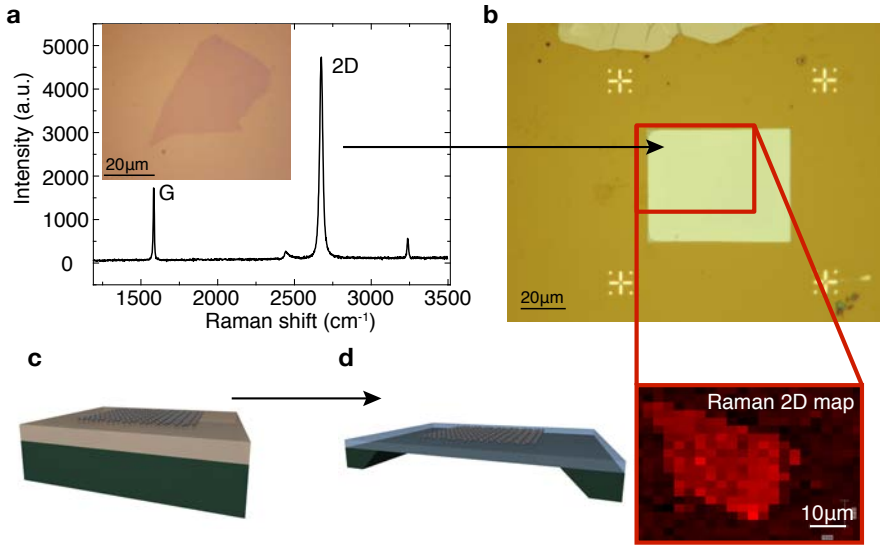

Figure 4.3: Exfoliation and transfer of single layer graphene. (a) Raman spectrum of an exfoliated, single-layer graphene flake. Inset: Optical microscope image of the exfoliated single layer graphene on Si/SiO_2. (b) Optical microscope image of single-layer graphene after transfer on to 50nm Si_3N_4 membrane. Also shown is a spatial map of the 2D Raman intensity confirming the successful transfer. (c) and (d) 3D visualizations of single layer graphene after exfoliation and transfer on to the target substrate.

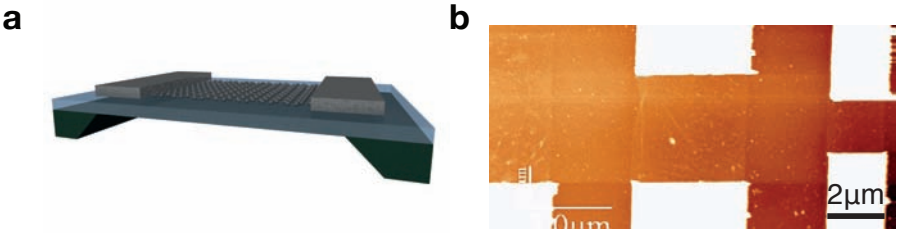

Figure 4.4: (a) 3D visualization of transferred graphene contacted by metallic leads. (b) atomic force microscope image acquired in tapping mode showing contacted graphene after patterning.

devices electrically accessible we pattern openings over the large contact pads by e-beam lithography and etch away the Al_2O_3 in 40% phosphoric acid by weight at a temperature of $T = 50°C$ (etch rate $\approx$ 5nm/min) using the PMMA resist as the etch mask (see Fig.4.6).

Cavity mirrors are prepared by depositing a 30nm Ag(Au) globally on the backside of the sample by e-beam evaporation. An additional

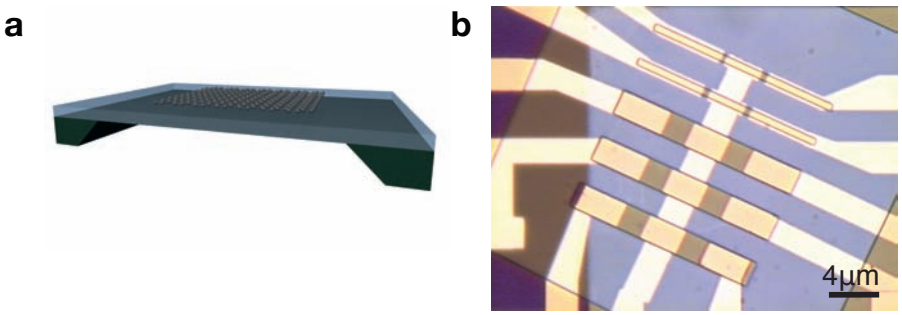

Figure 4.5: (a) 3D visualization of patterned graphene. (b) optical microscope image showing contacted graphene covered with a patterned PMMA mask used for selective O_2 plasma etching.

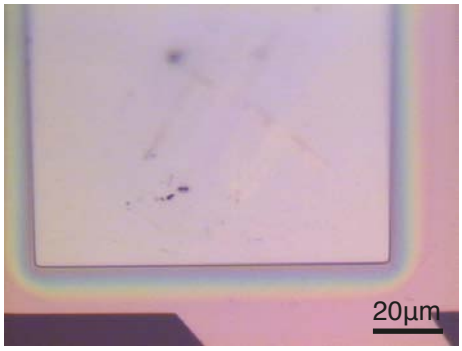

Figure 4.6: Optical microscope image after an isotropic Al_2O_3 etch masked by PMMA in 40% phosphoric acid by weight at a temperature of $T = 50°C$. The multicolor interference at the edge of the PMMA mask signifies etching underneath the PMMA.

e-beam lithography step is necessary for the local definition of the top cavity mirror followed by deposition of 60nm Ag(Au) to ensure the devices can still be addressed electrically. This finalizes the fabrication process with samples now being ready for further characterization

4.1.1 *Simulation and experimental verification of resonance wavelength and cavity-Q*

Before moving to the device characterization we like to elaborate on the level of control of the microcavity resonance wavelength by tuning the intra-cavity medium. The microcavity resonance is determined by the thickness of the Si_3N_4 and Al_2O_3 layers, i.e. the total thickness of

the intra-cavity medium. In our case the Si_3N_4 layer thickness is fixed at 50nm while the thickness of the second intra-cavity medium Al_2O_3 can be freely adjusted. To determine the Al_2O_3 thickness to grow, we modeled the cavity resonance within a transfer-matrix approach [65], i.e. a plane wave propagates through this multilayered cavity system and the electric field is evaluated at each boundary (see Fig. 4.7a). From the simulations we infer the proper Al_2O_3 thickness for a targeted cavity resonance wavelength (Fig. 4.7b). For validation of the simulations we built a series of reference cavities without graphene. The results in Fig. 4.7c demonstrate the level of control over the cavity resonance by adjusting the thickness of the alumina layer[3]. The cavity resonance profiles are measured in reflection with an FTIR microscope[4]. We attribute the difference in slope between measured and simulated cavity resonance wavelength to different assumptions of the optical constants of the layer materials in the simulations and when measuring the layer thickness by reflectometry. The cavity-Q values achieved (see Fig. 4.7d, Fig. 4.8) are in agreement with previous reports on planar cavities with metallic mirrors, where the Q factor is limited by absorption in the metallic mirrors [66].

4.2 ELECTRICAL AND OPTICAL CHARACTERIZATION

In the following sections we report on the device characterization by electronic, optical, and optoelectronic measurements to test the integrity of our samples.

Figure 4.9a outlines our novel integration principle: An electrically contacted single layer of graphene is embedded between two opti-

3 Alumina layer for reference samples have been deposited by using a Cambridge Nanotech Inc., Savannah 100 system. Access to this equipment is kindly provided by the group of Prof. Hahn, Institute of Nanotechnology, Karlsruhe Institute of Technology.

4 Measurements have been carried out in the group of Prof. Wegener, Institute of Applied Physics. Karlsruhe Institute of Technology with assistance from Prof. Stefan Linden, University of Bonn.

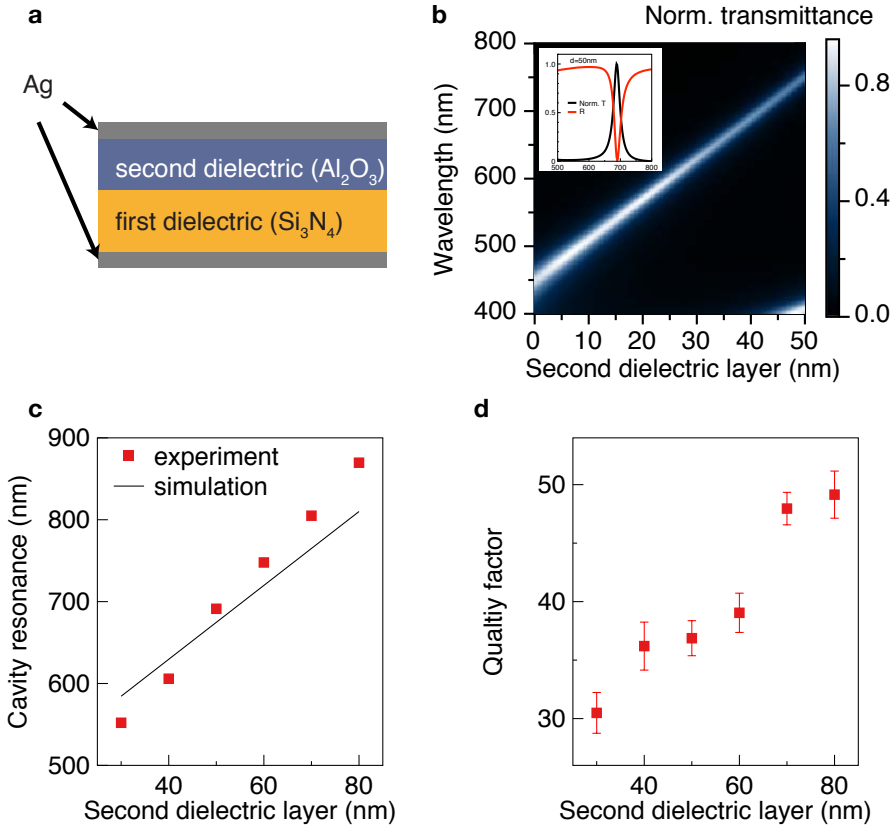

Figure 4.7: Simulation and design of the optical microcavity. (a) Schematic of the multilayer stack used for modeling the transmittance/reflectance of the microcavity as a function of wavelength and dielectric layer thickness. (b) False-color plot of the normalized transmittance of the cavity shown in (a). (c) Cavity resonance wavelength obtained by measuring the reflectance from reference cavities with Al_2O_3 layer thickness between 30nm and 80nm. Each data point represents the average of four different cavities. The solid line is a result from the optical simulation shown in (b). (d) Cavity-quality factors of the reference samples shown in (c). Each data point represents the average of four different cavities.

cally transparent, dielectric thin films made of Si_3N_4 and Al_2O_3, respectively. The dielectric layers are enclosed by two metallic (Ag, Au) mirrors with a spacing L that determines the resonance wavelength λ_{cavity} of the microcavity (see Ref. [58]). A novel multi-step manufacturing process (see section 4.1) allows us to define device area and cavity mirror spacing with nanometer precision and to build a series

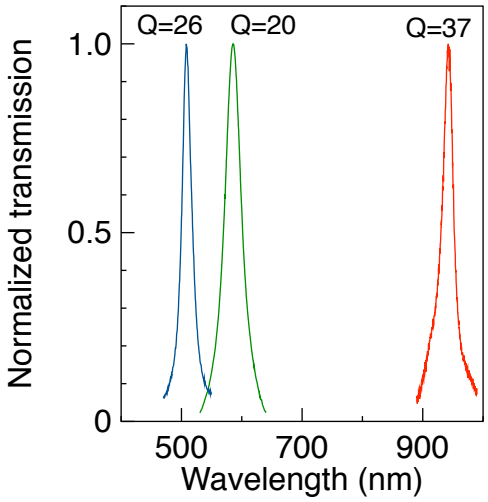

Figure 4.8: Overview of experimental transmission spectra taken from three representative devices designed for different experimental applications. The cavity-emitter discussed in the main text has the $\lambda/2$-resonance at 925nm (red curve); the spectrum with the $\lambda/2$-resonance at 600nm (green curve) is taken from the device used for performing the photocurrent spectroscopy. Also indicated are the corresponding cavity-Q factors.

of devices that satisfy the specific requirements of different optoelectronic experiments. For photocurrent studies, we designed the cavity resonance to match the tuning range of the laser system at hand ($\sim$ 580nm). For thermal emission studies, we designed the cavity resonance to be spectrally located within the detection range of the spectroscopic unit ($\sim$ 925nm). In principle, all the measurements can be performed on the same device while the efficiency of light absorption and emission are largely determined by the optical properties of the cavity.

4.2.1 *Electrical transport*

In order to characterize the electronic device properties, we measure both electrical transfer (Fig. 4.10a) and output characteristics (Fig. 4.10b) of the integrated graphene transistor. We apply a bias voltage

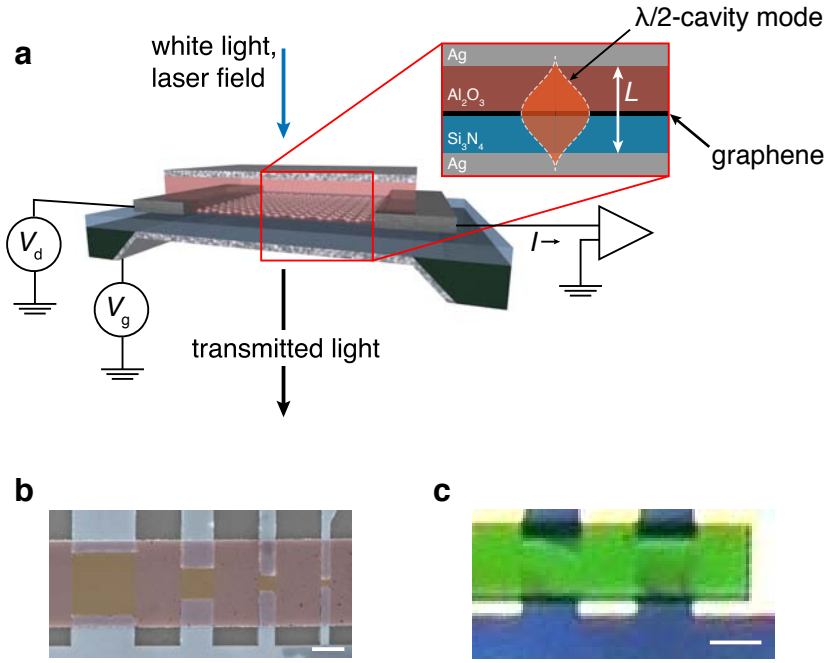

Figure 4.9: (a) Schematic representation and electrical interconnection of the device. (Inset) Cross sectional view of the device. The graphene sheet is embedded between two Ag mirrors and separated by two dielectric layers (Si_3N_4; Al_2O_3). The thickness L of the dielectric stack between the cavity mirrors determines the resonance wavelength λ of the optical microcavity. Also shown is the optical field profile of the fundamental $\lambda/2$ cavity mode. (b) Top-view scanning electron microscope false color image of the device; graphene sheets (yellow), Pd contacts (blue) Ag mirror (red). Scale bar, 2μm. (c) Optical white light transmission micrograph of the device. The fundamental cavity mode is spectrally located at $\lambda_{cavity} = 585$nm which appears green to the eye. Scale bar, 4μm.

along the graphene sheet and use one of the metallic cavity mirrors as a gate electrode (Fig. 4.9a). We fit the measured electrical transfer characteristics based on the model reported in Ref. [67]. There the total resistance R_{tot} of a graphene device is the sum of the contact resistance R_c and the graphene resistance R_{gr} that can be tuned with

an external gate electrode. The resistance of the graphene channel can be expressed as follows,

$$R_{gr} = \left(\frac{W\sigma}{L}\right)^{-1} = \left(\frac{We\mu_{FE}n_{tot}}{L}\right)^{-1} = \left(\frac{eW\mu_{FE}\sqrt{n_0^2 + n^2}}{L}\right)^{-1} \quad (4.2)$$

where W and L are the width and length of the graphene sheet, σ is the conductivity, e is the electrical charge, μ_{FE} is the field-effect mobility, and n_{tot}, n_0, and n are the total charge carrier density, residual charge carrier density, and gate induced charge carrier density, respectively. The residual carrier concentration n_0, which ideally in pristine graphene layer should be zero, stems from charged impurities [68] located either in the dielectric or at the graphene/dielectric interface. The gate-induced charge carrier density can be calculated from

$$V_g - V_{g,0} = \frac{en}{C_g} + \frac{\hbar v_F\sqrt{\pi n}}{e} \quad (4.3)$$

where the V_g is the gate voltage, $V_{g,0}$ is the gate voltage at the Dirac point, C_g is the geometric gate capacitance, and v_F is the Fermi velocity. The first term in Eq. 4.3 describes the electrostatic contribution and the second term comes from the finite quantum capacitance. R_{tot} then reads

$$R_{tot} = R_c + \frac{L}{We\mu_{FE}\sqrt{n_0^2 + n^2}} \quad (4.4)$$

and allows us to extract the device parameters that demonstrate the quality of the graphene sheet and the Pd-graphene contacts: We find a carrier mobility $\mu_{FE} = 2350\text{cm}^2\text{V}^{-1}\text{s}^{-1}$, a residual carrier density $n_0 = 4.9x10^{11}\text{cm}^{-2}$, an electrical- resistance ratio $R_{max}/R_{min} = 5$, and a specific contact resistance $R_c = 0.265\text{k}\Omega\mu\text{m}$ for the device shown in Fig. 4.10a.

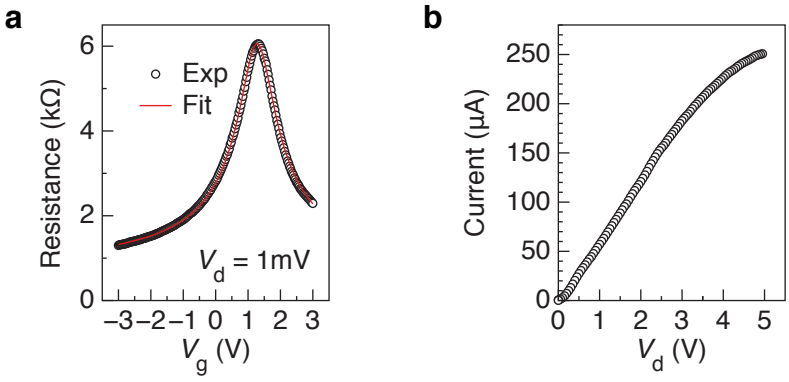

Figure 4.10: Electrical transfer (a) and output characteristics (a) of one of the devices.

4.2.2 *White light transmission spectroscopy*

In order to characterize the optical properties of the device, we illuminate the cavity with white light from the top (see Fig. 4.11a) and spectrally analyze the transmitted light. This way, we determine the resonance wavelength λ_{cavity} and the cavity quality factor $Q = \lambda_{cavity}/\Delta\lambda_{cavity}$, where $\Delta\lambda_{cavity}$ is the spectral full-width-at-half-maximum of the peak at λ_{cavity} in the measured transmission spectrum. In the present case (Fig. 4.11b), we obtain $\lambda_{cavity} = 585$nm and cavity-$Q \approx 20$.

4.2.3 *Photocurrent spectroscopy*

We employ photocurrent generation in graphene [69] to probe electronically the optical absorption of the graphene layer inside the device. We focus a laser beam on one of the microcavity mirrors, tune the laser wavelength across the optical resonance, and measure the photocurrent generated inside the biased graphene layer by means of a lock-in technique.

The functional dependence of the photocurrent amplitude on laser wavelength (Fig. 4.12b, red circles) matches the spectral profile of the cavity resonance as measured by white light transmission spec-

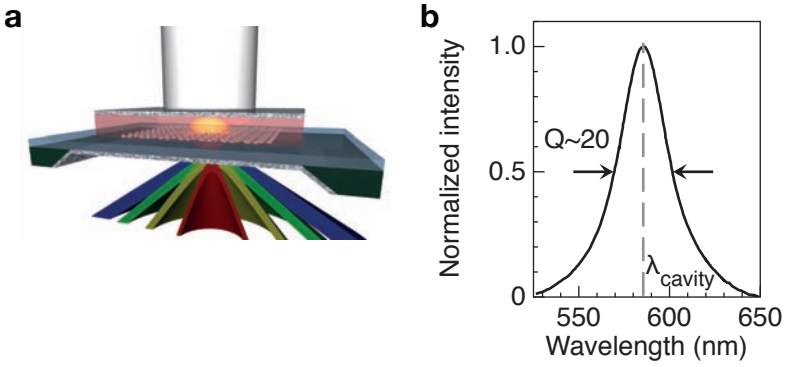

Figure 4.11: (a) 3D visualization of the measurement scheme. An approximately plane wave white light source impinges on the sample and the transmitted light is spectrally analyzed. The colored light cones indicate the blue shift of off-axis transmitted light. (b) Normalized transmission spectrum of a microcavity integrated graphene transistor; this transmission spectrum corresponds to the green spectrum in Fig.4.8.

troscopy (Fig. 4.12b, solid line). By tuning the laser wavelength to $\lambda_{laser} = 583$nm, on resonance with the microcavity, we obtain a photocurrent amplitude of 23.3nA, while we measure only 1.2nA for laser illumination at $\lambda_{laser} = 633$nm. This demonstrates that the device acts as light detector with spectral selectivity. In contrast, the photocurrent amplitude of a non-confined graphene transistor varies by less than a factor of 2 if we tune the laser excitation wavelength across the same spectral interval. The measured spectral dependence of the photocurrent in Fig. 4.12b is the result of two effects: the resonance distribution of the laser field inside the microcavity and, to a much lesser extent, the cavity-induced (Purcell) enhancement of graphene's absorption rate. To expand on this point the cavity-induced modifications of graphene absorption refer to the enhancement of graphene's intrinsic absorption rate. Based on the physical dimensions and optical parameters (effective index of refraction $n \approx 1.8$, cavity length

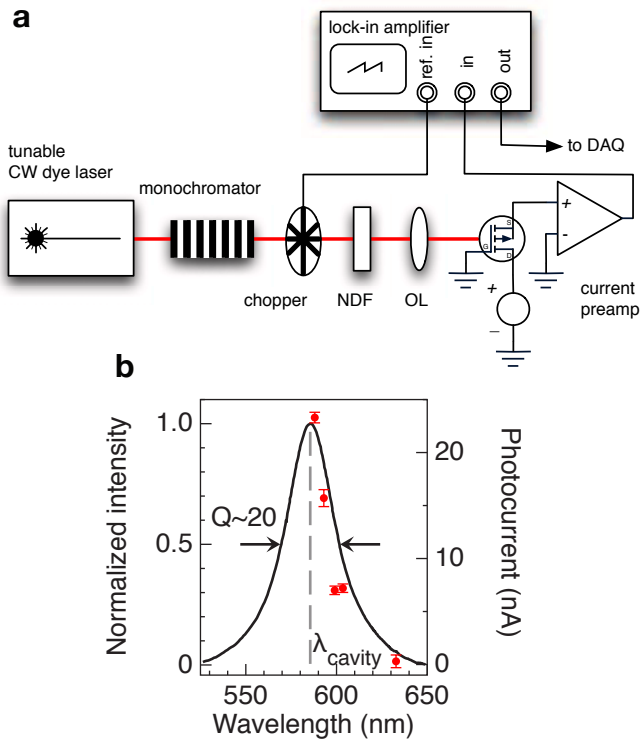

Figure 4.12: (a) Schematic of the experimental setup for performing photocurrent spectroscopy (ND: neutral density filter, OL: objective lens). (b) Photocurrent as a function of wavelength (red circles) overlaid with the transmission spectrum (solid line).

$L = 155$nm, and a mode diameter of $2r = 0.8\mu$m), the Purcell enhancement factor

$$P = \frac{3}{4\pi^2}\left(\frac{\lambda}{n}\right)^3 \frac{Q}{V} \tag{4.5}$$

is estimated to be in the range of 2 to 4 for our devices. As a result, in agreement with Ref. [6], the laser field enhancement due to the optical resonance is mainly responsible for the observed spectral dependence of the photocurrent. Strong-coupling effects are not expected due to the rather low Q factors in the present device configuration.

4.3 CAVITY CONFINED ELECTRICALLY EXCITED LIGHT EMISSION

We now investigate the light-emission properties of non-confined graphene and compare it to the microcavity-controlled graphene transistor.

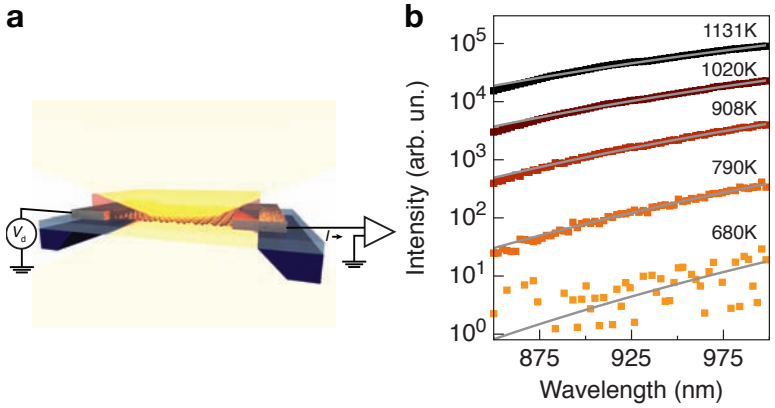

Figure 4.13: (a) Schematic visualizing how thermal light emission is generated by applying a drain bias. (b) Thermal near-infrared emission spectra measured for a non-confined graphene transistor.

By applying a bias voltage across the non-confined graphene device using source and drain electrodes (Fig. 4.13a), the electrical current heats up the graphene layer and thermal light emission sets in, as reported previously [52, 53]. As shown in Fig. 4.13b, the electrically excited, thermal emission spectrum of graphene in free, non-confined space exhibits a featureless exponential tail that shifts from the near-infrared towards the visible spectral range as a function of injected electrical power. The temperature values are extracted by fitting the measured emission spectra based on a model of a two-dimensional black-body radiation [70],

$$u(\lambda, T) = \epsilon \frac{4\pi hc}{\lambda^4} \frac{1}{\exp\left[\frac{hc}{\lambda k_B T}\right] - 1} \tag{4.6}$$

where ϵ is the emissivity, h is Planck's constant, and c is the speed of light.

In contrast, the thermal emission spectrum of a microcavity-controlled graphene transistor displays a single, narrow peak at $\lambda_{cavity} = 925\text{nm}$ having a full-width-at-half-maximum (FWHM) of 50nm (Fig. 4.14b), yielding a 140-fold spectral narrowing as compared to the simulated free-space thermal spectrum at $T = 650\text{K}$.

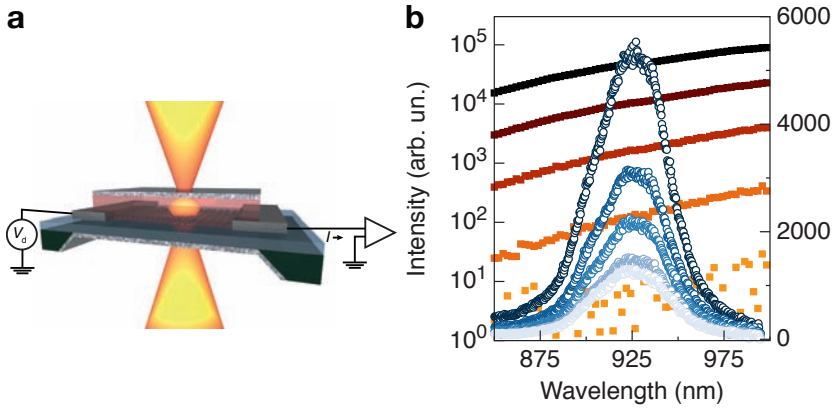

Figure 4.14: (a) Schematic visualizing how thermal light emission is generated by applying a drain bias and how thermal radiation couples to the optical cavity mode. (b) Thermal near-infrared emission spectra measured for a cavity-confined (open circles) and a non-confined (filled squares) graphene transistor. The emission spectra of the cavity-controlled graphene transistor displays the optical resonance of the cavity at $\lambda_{cavity} = 925\text{nm}$.

It is important to note that this is not merely a spectral filtering effect, but that thermal radiation cannot be emitted by the graphene layer at all if the thermal radiation wavelength $\lambda_{thermal}$ is larger than λ_{cavity} because of optical confinement, or, in other words, the cavity-induced inhibition of spontaneous emission. This constitutes the first demonstration of a electrically-driven, microcavity-controlled thermal light source. The spectral peak position of the emission peak does not shift as a function of injected electrical power. This observation points towards an insignificant heating of the dielectric layers surrounding the graphene sheet. We carried out a series of control experiments to substantiate this claim in subsection 4.3.1 and 4.3.2. The simulated emission spectra in Fig. 4.15a reproduce the overall shape of their ex-

perimental counterparts very well. Emission spectra have been simulated by superimposing a Lorentzian lineshape (center wavelength $\lambda = 925$nm and FWHM of 50nm) on the 2D black-body distribution. The integral over the microcavity-controlled light intensity is plotted as a function of the injected electrical power in Fig. 4.15b for three different devices. The power dependences reveal that the integrated light intensity is proportional to T^3 as expected from the Stefan-Boltzmann law of a two dimensional black-body radiator [70]. Here we assume that the electrical power density $p \propto T$ which is validated by measurements in non-confined space (see Fig.4.25). We attribute the non-systematic dependence with device area to microscopic inhomogeneities, i.e. varying defect density, across the graphene layer.

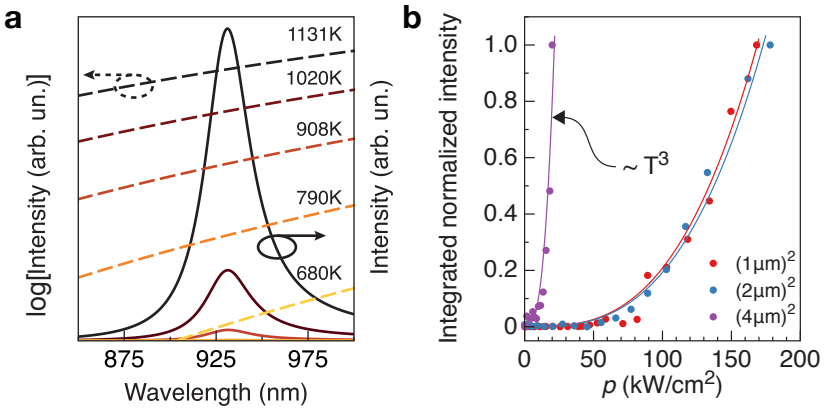

Figure 4.15: (a) Simulated thermal emission spectra of microcavity-controlled thermal radiation (solid lines) and a non-confined graphene transistor (dashed lines) modeled by assuming that the cavity resonance is spectrally located at $\lambda_{cavity} = 925nm$ and has a full-width-at-half-maximum of $30nm$. (b) Spectrally integrated light intensity as a function of electrical power density for three devices with different areas. The solid lines are T^3 fits assuming that the dissipated electrical power density is proportional to the temperature T in the graphene sheet.

We now establish the physical concept of cavity-controlled thermal light generation in graphene. The graphene layer initially heats up due to carrier scattering. The emission of long-wavelength thermal ra-

diation at $\lambda_{thermal} > \lambda_{cavity}$ is however inhibited by the cavity. As the temperature in the graphene sheet increases as a function of the electrical power density p, the thermal distribution inside the graphene layer spectrally shifts towards λ_{cavity} (Fig. 4.14b) and, at a threshold temperature T_{cavity}, eventually enables the emission of a significant fraction of photons at $\lambda_{thermal} \leq \lambda_{cavity}$. We note that the temperature T_{cavity} and the corresponding threshold power density p_{cavity} depend on device parameters, i.e., the carrier mobility μ, the channel area, and λ_{cavity}. For the device in Fig. 4.14b, we find $T_{cavity} = 650K$ and $p_{cavity} = 90kW/cm^2$. The connection between temperature T and power density p has been established by Freitag et al. [71] using Raman thermometry. Based on Wien's law in two dimensions [70] we estimate that the graphene layer would have to be heated up to $T_{cavity,optimum} \approx hc/3.92k_B\lambda_{cavity} \approx 4000$K in order to maximize the light output at $\lambda_{cavity} = 925$nm. In this case, the intensity maximum of the thermal- radiation distribution would overlap with the cavity resonance at λ_{cavity}, resulting in a peak population of the cavity mode by thermal photons. Note that we designed microcavity devices specifically for performing the thermal emission spectroscopy in the near-infrared in order to take advantage of the favorable experimental conditions, i.e. the high sensitivity and detection yield of the CCD array at hand. The optimum light-emitting performance, however, is expected to be in the mid-infrared spectral range. Assuming device operation at, for example, $T_{cavity} = 650$K, we estimate a maximum thermal light output at $\lambda_{thermal} \approx 5.6\mu$m. Future work should hence extend the spectral range towards the terahertz regime.

4.3.1 *Heat induced cavity resonance shifts*

As pointed out in section 4.3 we do not observe a spectral shift of the emission peak which led us to conclude that there is a insignificant heating of the intra-cavity dielectrics. One would naively expect, that

a change in temperature and therefore a change in the optical properties and the accompanying thermal expansion of the intra-cavity media can cause a shift in the resonance wavelength of the cavity. For that reason we perform white light transmission spectroscopy under external heating of the cavity with and without graphene integrated into the cavity stack. In both cases we observe a red shift of the cavity resonance under external heating. From this observation we conclude that there is only a weak thermal coupling of the graphene to its dielectric environment considering that an expected red shift is not observed for cavity confined thermal emission or transmission in contrast to the situation for external heating.

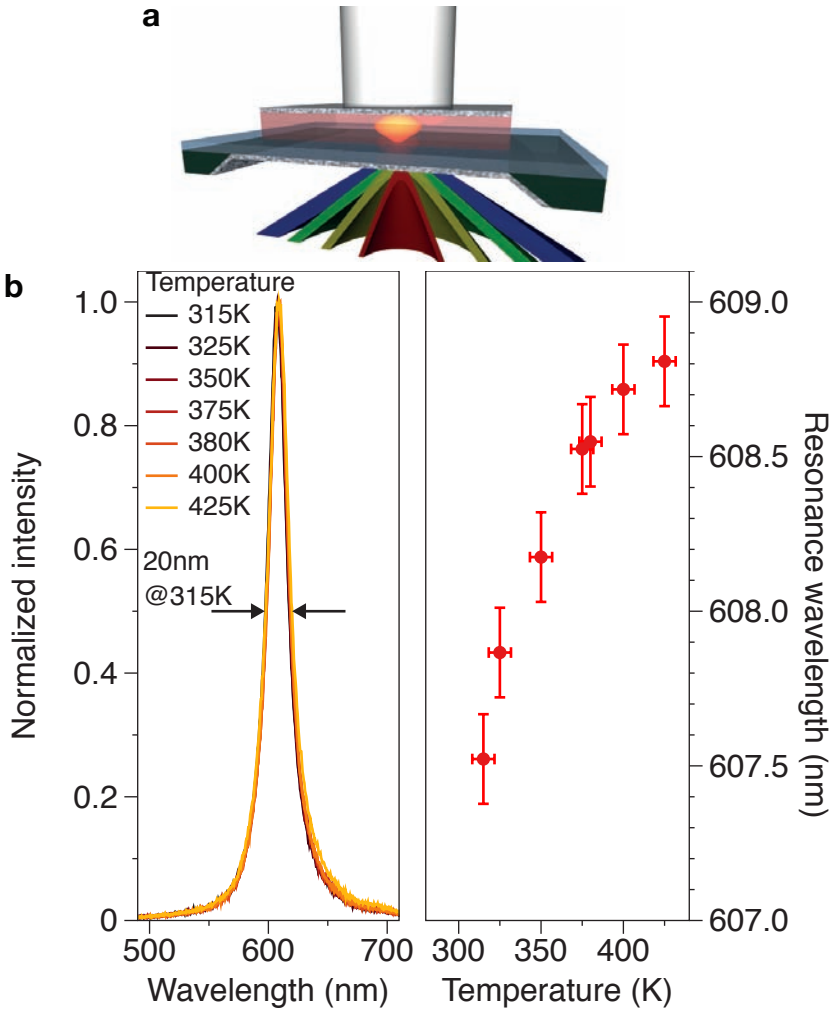

Figure 4.16: (a) 3D visualization of light transmission through a microcavity without graphene. (b) The left hand side shows the normalized transmission spectra as a function of temperature. The right hand side presents the extracted resonance wavelength as a function of temperature.

4.3.2 *Power induced cavity resonance shifts*

In a second set of control experiments we measure the transmission through cavity-integrated graphene transistors as a function of the dissipated electrical power density. To this end we apply a DC voltage bias to the graphene device and monitor the resulting current flow. At each bias point we acquire a transmission spectrum of the cavity and extract the resonance wavelength. In figure 4.18 we plot the results

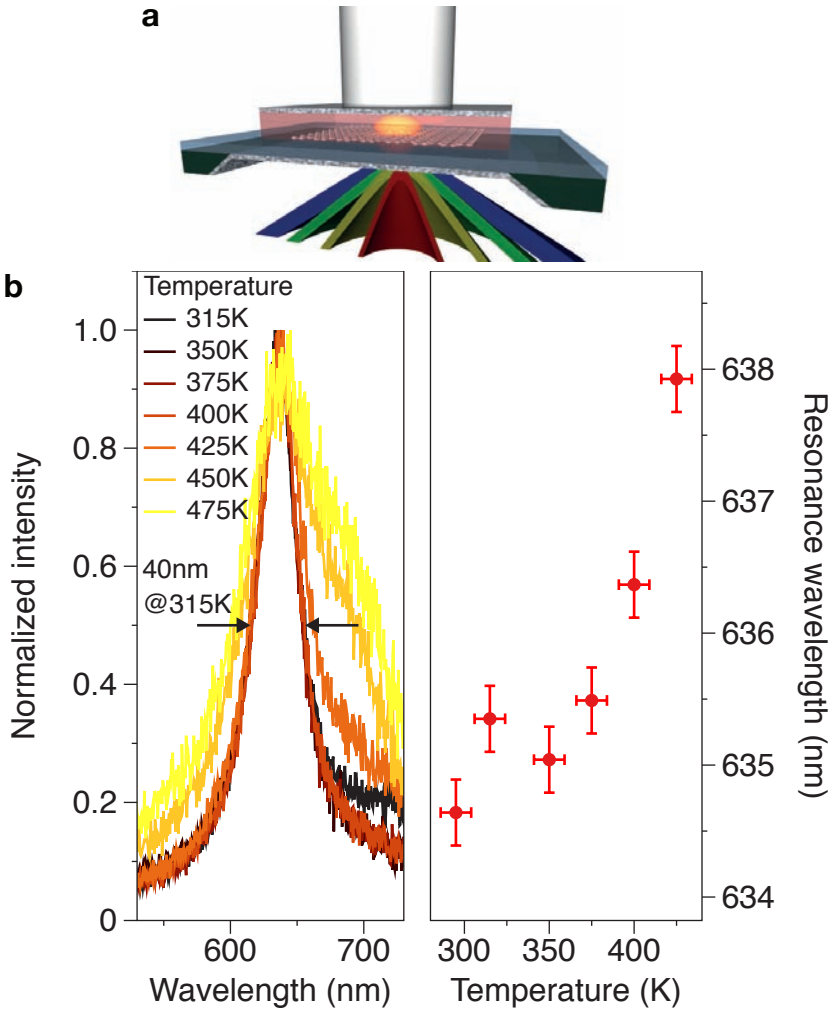

Figure 4.17: (a) 3D visualization of light transmission through a microcavity with graphene. (b) The left hand side shows the normalized transmission spectra as a function of temperature. The right hand side presents the extracted resonance wavelength as a function of temperature.

for three devices with different active areas ($4x4\mu m^2$, $2x2\mu m^2$, and $1x1\mu m^2$) for the first- and second-order cavity mode. We consistently observe a blue shift of the cavity resonance that linearly scales with dissipated electrical power density. At this point we are not able to provide an explanation for this spectral blue shift under power dissipation inside the graphene sheet. Further measurements and theory support are thus needed to elucidate this experimental observation.

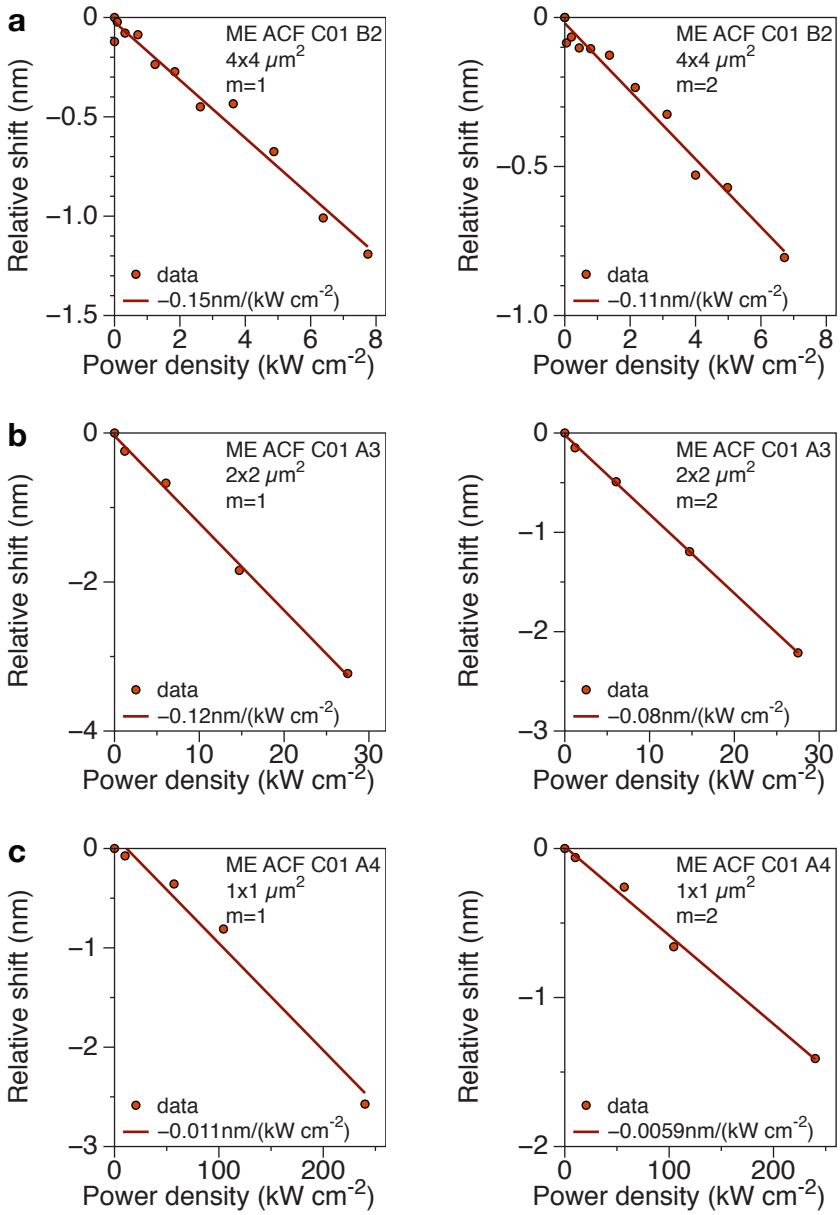

Figure 4.18: Power induced cavity resonance shifts with graphene. Relative shift of the cavity resonance wavelength as a function of the dissipated electric power density for devices with a device area of (a) $4x4\mu m^2$, (b) $2x2\mu m^2$, and (c) $1x1\mu m^2$.

4.3.3 *Possible piezoelectric induced cavity resonance shifts*

We want to exclude cavity resonance shifts that are caused by piezoelectric effects of the intra-cavity dielectrics or simple compression by electrostatic attraction between metallic contacts under applied bias

voltage that may alter the cavity dimensions. For that reason we measure the transmission of white light through cavity devices identical to those described in section 4.1 but without graphene. Transmission spectra have been acquired as a function of applied bias voltage between open contact pairs spaced 4μm apart for the first ($m = 1$) and second ($m = 2$) cavity mode. The measurement scheme and results are plotted in Fig. 4.19. The intention here is to exclude changes in the cavity dimensions and consequently its resonance wavelength caused by piezoelectricity of the Si_3N_4 intra-cavity layer. In Fig. 4.19 we show that within the experimentally accessible voltage range no change in the resonance wavelength for the first and second cavity mode is observed.

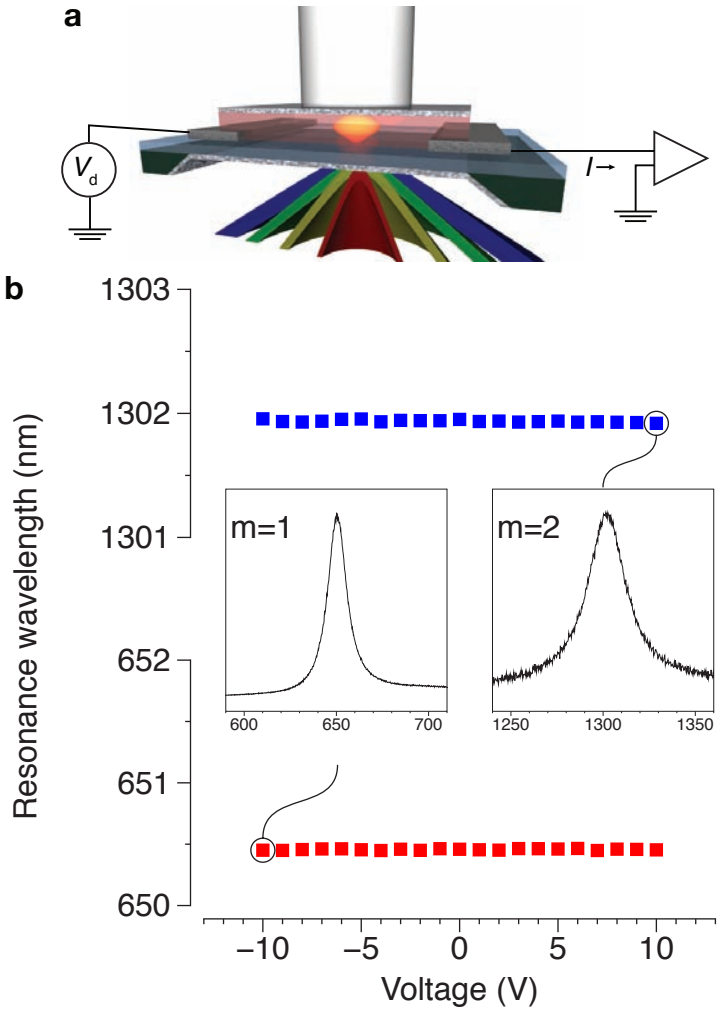

Figure 4.19: (a) 3D visualization of light transmission through a microcavity with graphene and external circuitry. (b) Resonance wavelength of the first- and second-order cavity mode as a function of applied bias between contacts indicated in (a).

4.3.4 *Microcavity-controlled thermal emission - angular distribution*

We now analyze the angular distribution of the cavity-confined thermal light emission. Based on the theory of multi-beam interference inside a Fabry-Perot cavity one can deduce the following equation

that relates the emission wavelength λ to the emission angle θ with respect to the cavity normal (see Fig. 4.20),

$$\lambda = \frac{2Ln}{(m - \Delta\phi/2\pi)} \cos\theta \tag{4.7}$$

where L is the geometrical mirror spacing (or cavity length), n is an effective refractive index of the intra-cavity medium, m is the mode order ($m = 1$ in this case), and $\Delta\phi$ is the phase shift associated with light absorption in the metallic mirrors. The microscope objective used in our measurements has a numerical aperture of $NA = 0.8$. This corresponds to a maximum detection angle of $\theta_{max} = 53.1^\circ$ with respect to the cavity normal (see Fig. 4.20).

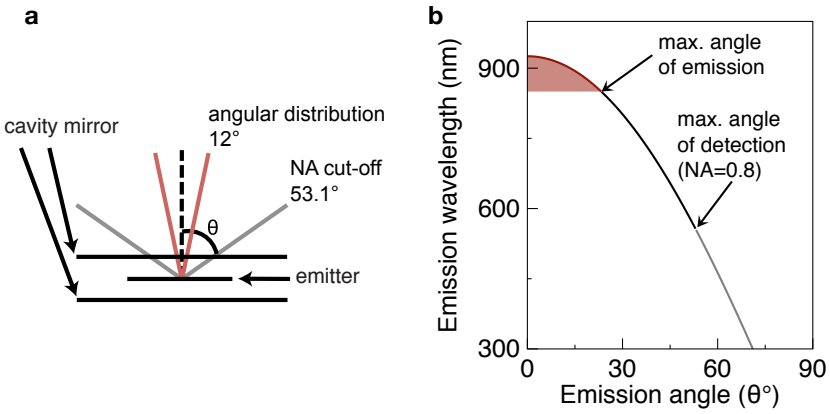

Figure 4.20: Detection of cavity-confined thermal emission. (a) Schematic showing the graphene layer placed between the two cavity mirrors. Also indicated are the maximum angle of detection and the angular distribution of the emitted light. (b) Emission wavelength as a function of emission angle. No light emission can be observed for $\theta > 23^\circ$.

For the device discussed in figure 4.14, having an on-axis ($\theta = 0^\circ$) resonance wavelength of 925nm, the shortest wavelength that can be collected is 556nm. The measured microcavity-controlled emission spectra typically level off at around 850nm and have a spectral width of 40nm (FWHM), which translates into an angular distribution of $\Delta\theta = 12^\circ$ (FWHM), with an intensity maximum occurring at $\theta_{max} =$

5° (see Fig. 4.20). This demonstrates that the cavity-coupled thermal emission of graphene is radiated into a narrow lobe and that off-axis emission coupled to guided modes is insignificant.

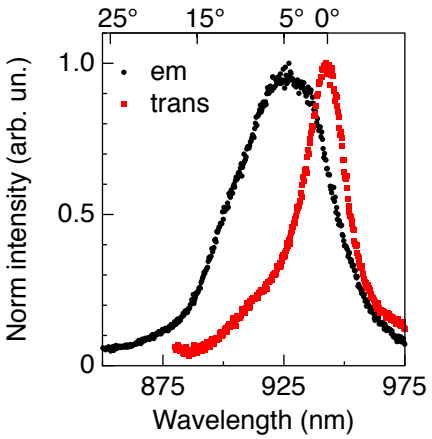

Figure 4.21: Angular distribution of microcavity-controlled thermal emission. On-axis transmission (red) and thermal emission (black) spectrum measured on the same device as a function of wavelength and emission angle, respectively. The maximum thermal emission intensity is observed at 5° and the collimated thermal emission lobe has an angular width of 12° (FWHM).

4.4 CAVITY-INDUCED MODIFICATIONS OF ELECTRICAL TRANSPORT

Finally, we discuss modifications of electrical transport in optically confined graphene that are related to the cavity-induced modifications of spontaneous thermal emission. Electrical transport in graphene depends on charge-carrier and phonon temperatures [52, 53]. Current-induced self-heating has been invoked to explain current saturation of graphene transistors in the high-field regime [72]. It is hence conceivable that the inhibition of spontaneous thermal emission for $\lambda_{thermal} > \lambda_{cavity}$, combined with the simultaneous enhancement of thermal radiation for $\lambda_{thermal} \leq \lambda_{cavity}$ may alter the efficiencies of thermal dissipation pathways in a way that the electrical trans-

port characteristics of the cavity-confined graphene transistor could be affected. In general, thermal emission is not the main heat dissipation channel in graphene [52]. However, the efficiency of the thermal emission channel could become significant for device operation and thermal management in the high-field transport limit where electrical current in graphene saturates.

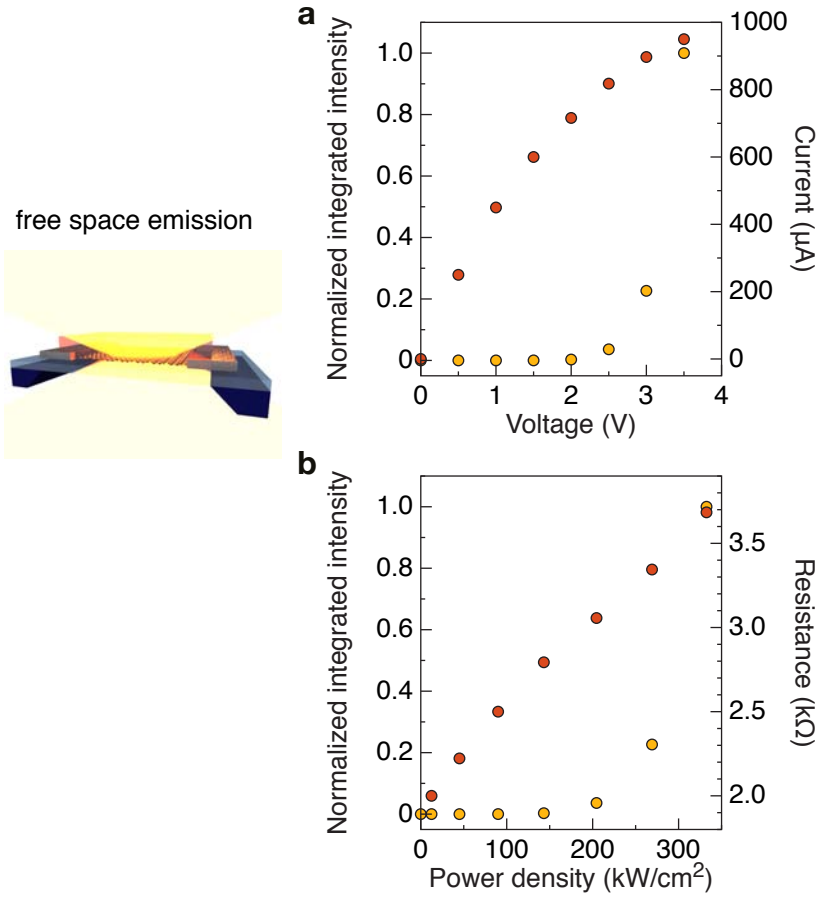

Figure 4.22: (a) Normalized and integrated, emitted light intensity (yellow) and electrical current (orange) as function of bias voltage measured with a non-confined graphene transistor. (b) Normalized integrated light intensity (yellow) and the electrical resistance (orange) are plotted as a function of electrical power density.

In Fig. 4.22, we show the electrical output characteristics of a graphene transistor in non-confined space. The electrical current in the graphene layer saturates in the high bias regime while thermal light emission sets in as it shifts into the detection range. The observed

current saturation is in agreement with reports in the literature for non-confined graphene devices in the high-current limit [73].

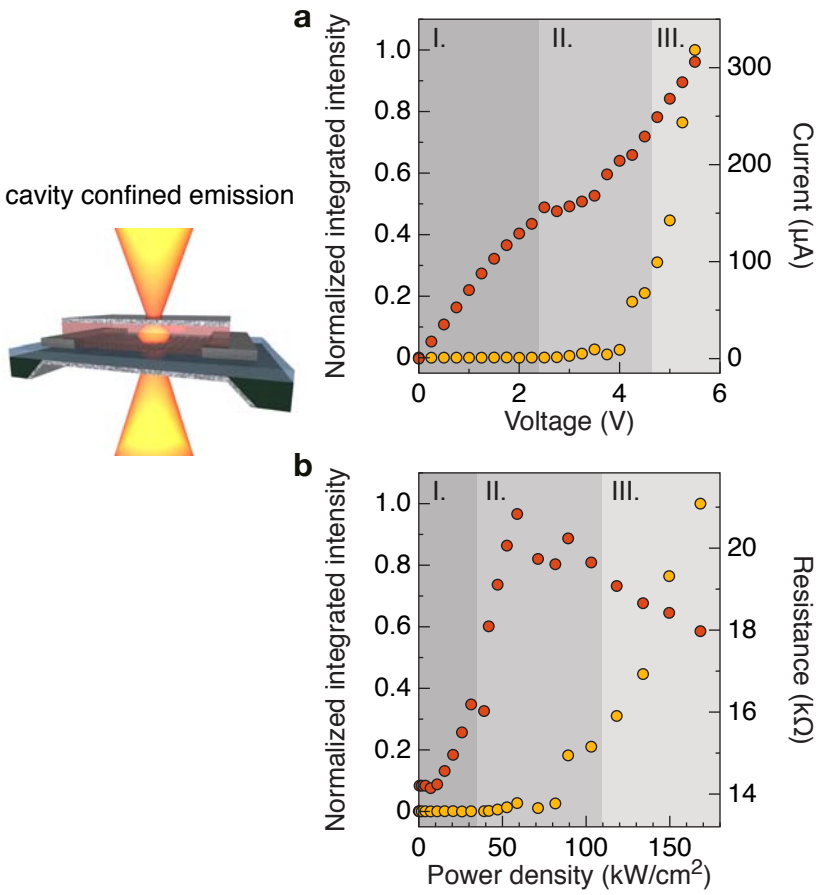

Figure 4.23: (a) Normalized integrated emitted light intensity (yellow) and electrical current (orange) as a function of bias voltage measured with a microcavity-controlled graphene transistor. Three regimes can be identified: (I.) sub-threshold, (II.) threshold and (III.) above-threshold, respectively. (b) Normalized integrated light intensity (yellow) and electrical resistance (orange) are plotted as a function of electrical power density.

Performing the same experiment for a cavity-controlled graphene transistor with identical dimensions, we find that the electrical output characteristic is qualitatively different (see Fig. 4.23) and we can identify three different regimes by comparing electrical transport and light emission properties. In the sub-threshold regime (I.), the electrical current saturates and the graphene layer heats up while the cavity-

induced inhibition of spontaneous emission for $\lambda_{thermal} > \lambda_{cavity}$ prevents off-resonant thermal radiation. In the threshold regime (II.), the temperature of the graphene sheet has reached the critical value T_{cavity} enabling light emission at $\lambda_{thermal} \leq \lambda_{cavity}$. In the above-threshold regime (III.), the cavity mode provides a significant power dissipation channel for thermal photons, because the initial electrical current saturation is lifted and the electrical resistance drops as function of electrical power density.

We have observed electrical transport modifications similar to those shown in Fig. 4.23 in all functional (five) graphene-cavity devices, i.e. those that allowed for thermal light generation. In all cases, the saturation currents in regime (I.) were lower than the saturation currents obtained in the non-confined reference devices (same contacts and dielectric layers, no metal mirrors). We can rationalize this observation if we assume that the onset of current saturation in graphene depends on temperature and that the degree of self-heating is determined by the thermal coupling of graphene to its local environment, captured by the thermal conductance r as suggested in Ref. [72]. The saturation current j in the graphene layer is then proportional to $\sqrt{r}$. This implies that cavity-induced variations of r with respect to the non-confined reference value r_0 will lead to variations of the saturation current j and, accordingly, to the temperature $\Delta T \propto j$ in the graphene layer.

In this scenario, the cavity-induced inhibition of the radiative thermal relaxation leads to enhanced self-heating of the graphene layer and an onset of current saturation at lower electrical power levels as compared to the non-confined case. Based on the experimental transport data and the self-heating model presented in Ref. [72], we estimate temperature differences as high as $\Delta T = 100$K when compared to the same graphene transistor in non-confined space, which will be discussed in section 4.4.1.

To expand on this point, modifications of the electrical transport in microcavity-controlled graphene transistors that are in qualitative

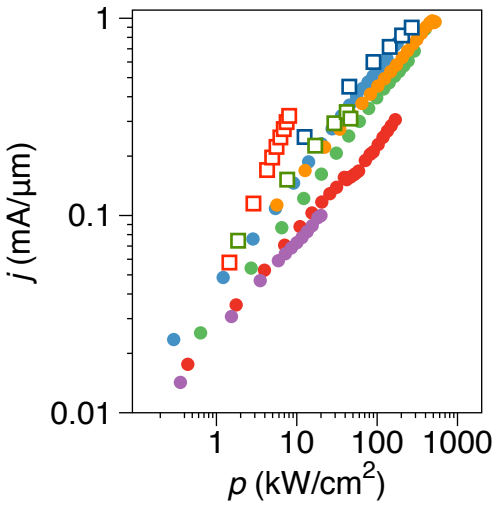

Figure 4.24: Comparison of electrical saturation current levels in confined and non-confined graphene transistors. The experimental saturation current density is plotted as a function of electrical power density for a total of eight graphene transistors. Microcavity-controlled graphene transistors (filled circles) consistently exhibit current saturation at lower electrical power densities than non-confined graphene transistors (open squares), along with a sudden increase of current density above threshold for thermal emission.

agreement with the data in Fig. 4.23 have been observed in a total of 5 devices. In all cases, the current density of microcavity-controlled graphene transistors saturates at lower electrical power levels than in the non-confined transistors (see Fig. 4.24). Also, a sudden increase of the current density above threshold for thermal light emission is only observed for microcavity-controlled graphene transistors (see Fig.4.23a).

4.4.1 *Estimating temperature effects in a microcavity-controlled graphene transistor*

As a consequence of the current device layout we are not able to provide a direct measurement of the device temperature by for example Raman spectroscopy [71]. Nonetheless, we try to provide an

estimate of temperature changes during microcavity-controlled thermal emission which is outlined in the following. At high source-drain bias, the saturation current density j_{sat} in graphene depends on the self-heating of the graphene layer [72]. The degree of self-heating is determined by the thermal coupling of graphene to its environment. A measure for the thermal coupling is the thermal conductance r. Within the self-heating model the saturation current is proportional to the square root of the thermal conductance,

$$j_{sat} \propto \sqrt{r} \tag{4.8}$$

We extract a lower bound for the thermal conductance r_0 in our graphene transistors by fitting in Fig. 4.25 the measured spectra of the free space, non-confined thermal radiation to the following expression

$$T = T_{amb} + \frac{jF}{r_0} \tag{4.9}$$

which yields $r_0 = 0.4\text{kW}/(\text{cm}^2\text{K})$ (F is the electric field).

We now estimate the temperature modifications ΔT associated with the optical confinement based on the expression

$$\Delta T = \frac{j_{sat}F}{r} \tag{4.10}$$

We assume that $j_{sat} = j - j_{sat,0}$ for $j > j_{sat,0}$ and that relative changes in the thermal conductance r can be captured through the relative changes of the saturation current

$$r = r_0 \left(\frac{j_{sat}}{j_{sat,0}} \right)^2 \tag{4.11}$$

As the reference saturation current density $j_{sat,0}$, we choose the current density at the intersection between regimes I. and II. (see Fig. 4.26).

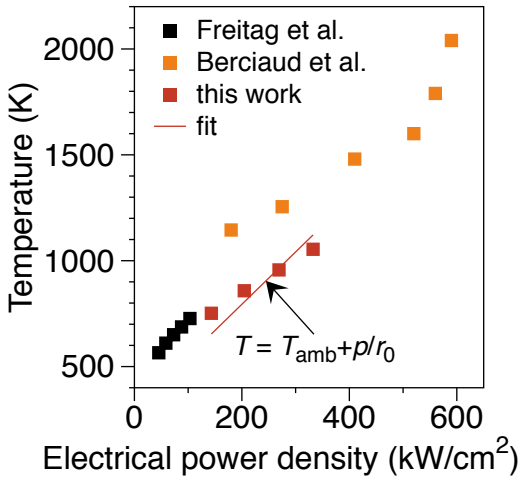

Figure 4.25: Temperature dependence of non-confined, free-space graphene transistors. Plotted is the temperature of graphene as function of injected electrical power density, in comparison with data taken from the literature [52, 53]. The temperature values are extracted by fitting the measured free space thermal emission spectra of a reference graphene transistor (with the same dielectric layers and metal contacts, but without cavity mirrors) to a model of a two-dimensional black body.

The resulting temperature modifications for the cavity emitter discussed in Figs. 4.14 and 4.23 are plotted in Fig. 4.26. As compared to graphene in free, non-confined space, the modification of the saturation current suggests temperature variations as high as $\Delta T = 100$K.

4.4.2 *Radiative energy dissipation and photon flux*

In order to estimate the rate at which heat is radiatively dissipated through cavity-controlled thermal light emission, we convert the measured light intensity into an energy flux. By summing the measured photon flux in the spectral window of the cavity resonance and taking into account the detection conditions, we obtain the integrated energy flow that emanates from the device area of 1μm^2 at each bias point. In Fig. 4.27 we present the results of this analysis. Above threshold

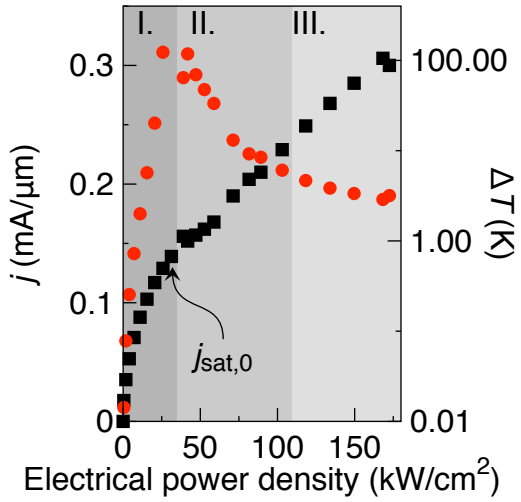

Figure 4.26: Temperature modifications of biased, cavity-confined graphene. Electrical current density (black squares) and relative temperature change (red circles) as function electrical power density. The cavity-confined graphene transistor heats up by ΔT as a consequence of the inhibition of thermal radiation (within regime I.). Once thermal radiation sets in (threshold regime II.), the temperature elevation decreases.

at 4V or 80kW/cm^2, respectively, the device emits thermal photons having energy of 1.3eV ($\lambda \approx 925$nm) which is equivalent to an overall heat transfer at a rate of $4.8x10^6$eV/s.

The ratio of the total electrical power density and the energy flux of thermal photons yields a factor of 10^9 which leaves us in a paradoxical situation. On the one hand we need a temperature change $\Delta T = 100$K to account for the changes in the current-voltage characteristics of cavity-confined graphene. On the other hand we know that only a tiny fraction of heat (10^{-9}) is dissipated by thermal radiation.

Hence, a model of the electrical transport and its temperature dependence in a microcavity-controlled graphene transistor is needed and should account for the current-induced self-heating of graphene that is affected by both (1) the non-radiative heat transfer through dielectric interfaces and metal contacts, and (2) the microcavity-controlled,

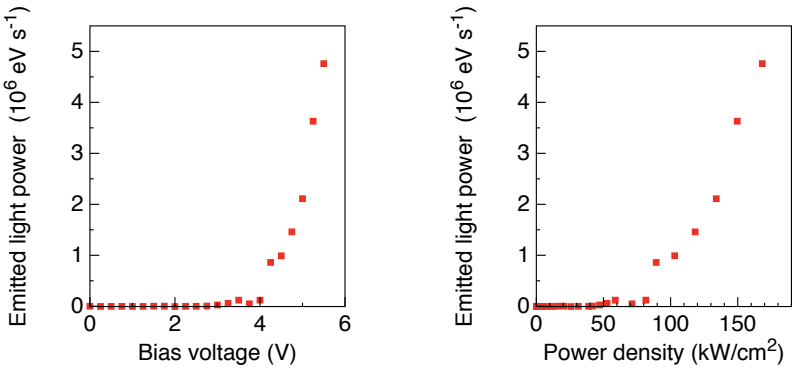

(a) (b)

Figure 4.27: Radiated heat flow as function of bias voltage and electrical power density. Microcavity-controlled, radiative heat dissipation rate per unit area as function of bias voltage applied. Above threshold at 4V and 80kW/cm^2, a significant amount of heat within the graphene layer is radiatively coupled to the microcavity.

radiative heat transfer by means of spontaneous emission of thermal photons.

4.5 CONCLUSION

In summary, we demonstrated that a microcavity-controlled graphene transistor can act as a spectrally selective light detector and emitter. Moreover, we found that the cavity-induced optical confinement modifies graphene's electrical transport characteristics, an effect with implications for nanoelectronics as well as cavity quantum electrodynamics.

5

HIGH-RESOLUTION POTENTIAL MAPPING OF CARBON NANOTUBE ARRAY PHOTODIODES

Semiconducting carbon nanotubes (CNTs) are a promising material for electronic and optoelectronic applications [32]. In electronics, CNTs are explored as a potential channel material for field-effect transistors [74]. Within an optoelectronic device, CNTs could take up various functionalities and perform as e.g. light absorbing and emitting layers [75, 76, 77, 78, 79, 80, 81], as the electrically conducting channel [82], and as (transparent) electrodes [83]. Several studies have been carried out with devices made of single CNTs [84, 85, 86], but ultimately single CNTs do not deliver sufficiently high current densities [86] or photon-to-carrier conversion yields [76] to become technologically relevant. It is hence necessary to extend those studies to CNT arrays [87, 88]. As is the case with devices made of single CNTs, the electronic performance of a CNT array is largely determined by the physics of CNT-metal contacts as with individual CNTs [89, 90]. The electrostatic potential deformation at CNT-metal contacts determines charge carrier injection efficiency [91] and is mainly responsible for the photovoltaic response observed [77]. However, previous optical studies on CNT devices have been restricted to the device channel, i.e. the area between the contacts, [77, 92], because the metal-CNT interface underneath the contacts was inaccessible. In order to be able to study CNT-metal contacts and the internal potential profile of CNT devices with high spatial resolution, it is necessary to use a transparent device that enables a complete optical inspection.

Here we investigate optically transparent CNT array devices in which CNTs act as the light absorbing layer and simultaneously promote the carrier separation and transport to metallic electrodes. We have implemented and investigated two different device concepts: (1) Metal-CNT-metal junctions in which a built-in electric field across the CNT array is achieved by using two different contact metals. The work function difference of the metals creates a built-in electric field across the CNT array (device channel) that separates electron-hole pairs (excitons) into free carriers at opposite contacts [93, 94]. (2) CNT array p-i-n junction devices with split top gates made of metal. In this case, we use electrostatic field doping through the local gates in order to create a potential drop across the CNT array, as demonstrated previously for single CNTs [84, 95, 96] and CNT arrays [97].

The optically transparent sample platform allows us to perform high-resolution, immersion-assisted photocurrent microscopy in functioning devices. We acquire photocurrent images of CNT array devices by raster scanning the devices with respect to a tightly focused laser beam. The photocurrent measurements provide insight into the internal potential profile of CNT array devices and allow us to directly measure the charge carrier transfer length at CNT-metal interfaces. Most importantly, the measurements reveal local potential heterogeneities that can affect the performance of the CNT array device as a whole. Furthermore, we monitor how electrostatic doping by a gate field can be used to control the local potential profile in a CNT array device.

5.1 SAMPLE FABRICATION

We fabricate transparent CNT film devices based on commercially available microscope cover slips having a size of $20x20\text{mm}^2$ that are coated with ITO (SPI Supplies). The ITO has a sheet resistivity of $6 - 8\Omega/\square$. The purpose of the ITO layer is twofold. Firstly, it can

be used as a global back gate electrode, and secondly, it serves as a charge dissipating layer mitigating charging effects during e-beam lithography. In a first step we deposit 50nm of Al_2O_3 by atomic layer deposition (ALD) on top of the ITO layer. In the next step, we assemble CNT films on top of the Al_2O_3 via a self-assembly method reported in Ref. [88]. In brief, the substrates are vertically immersed into highly purified ($>$ 99%) semiconducting CNT synthesized by the arc discharge method wrapped in SDS with a concentration of 0.1mg/ml [98, 99]. The CNT dispersion forms a pinning line on the sample surface that moves across the sample as the solvent evaporates, leaving behind areas with highly aligned CNT arrays. We then pattern a sparse grid of alignment markers by e-beam lithography onto the sample surface, followed by evaporation of 5nm Ti, 50nm Au, and a lift-off process step.

We manufacture CNT array devices with two different layouts:

1. Pd-CNT-Al junctions in which a built-in electric field across the CNT array is achieved by using two different contact metals.

2. Pd-CNT-Pd devices with split top gates made of metal on top of a thin insulator.

In (1), we perform two e-beam lithography steps for defining the first and second contact metal followed by evaporation of $1nm$ Ti/$30nm$ Pd/$30nm$ Au and $1nm$ Ti/$30nm$ Al/$30nm$ Au, respectively. In (2), only a single e-beam lithography step is necessary for patterning the contacts. In the next step, we coat all device sites with a local dielectric layer of $30nm$ Al_2O_3 by atomic layer deposition at lower temperature ($120^{\circ}C$) through a PMMA mask defined by e-beam lithography. The Al_2O_3 layer serves two purposes. Firstly, it is used as an etching mask to remove extraneous CNT material in an O_2-based plasma etching process step. Secondly, it serves as gate dielectric for the local split gates. The top gates made of $30nm$ Ti are produced with varying spacing ($0.25\mu m$, $0.5\mu m$, and $1\mu m$) in a final e-beam lithography step.

The spacing between the top gates determines the size of the intrinsic region in the p-i-n CNT film diode.

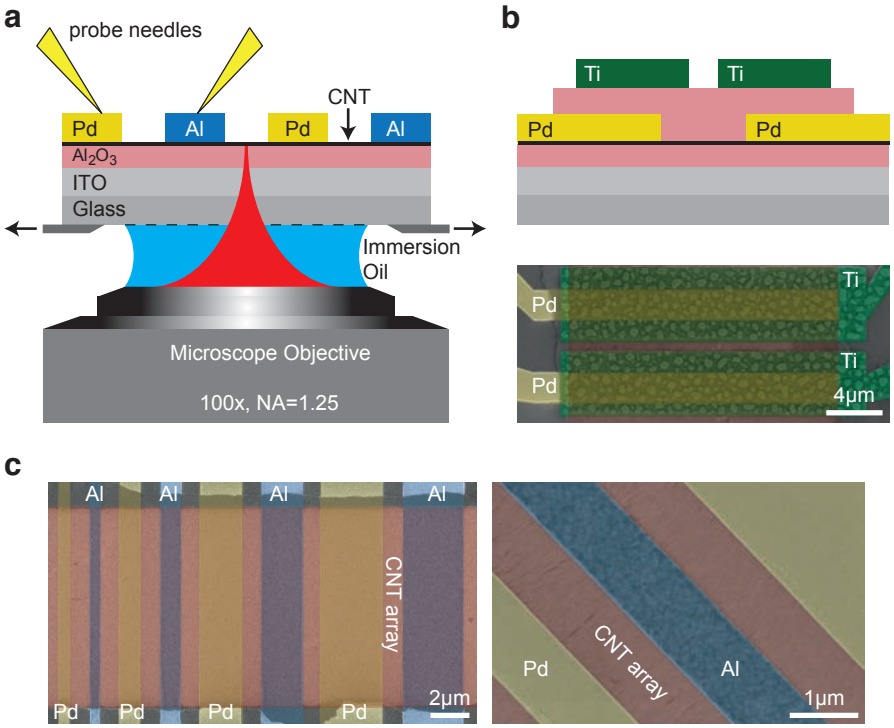

Figure 5.1: (a) Schematic of a CNT device built on an optically transparent multilayer substrate for studying photocurrent generation from the bottomside with an inverted scanning optical microscope. (b) Device schematic of a CNT array photodiode based on split top gates and false-color scanning electron microscope image of such a device (yellow: Pd electrodes, green: Ti split gates, and red: CNT array). (c) False-color scanning electron microscope images of a CNT array device with alternating contacts as schematically indicated in (a) (yellow: Pd electrodes, blue: Al electrodes, and red: CNT array). CNT density is estimated to be ca. 50CNT/μm.

Figure 5.1a shows our experimental setup and sample design. We use an inverted optical microscope in combination with a multi-axis scanning stage that allows for scanning the sample with respect to a tightly focused laser spot with nanometer precision. The sample mount is equipped with DC probes that are used for addressing the devices electrically. For photocurrent measurements, we convert the short-circuit photocurrent between the source and drain (ground)

electrodes into a voltage signal by using a current preamplifier and a source meter that are synchronized with a controlling computer and the optical scanning system. Control of bias conditions and electronic transport measurements were accomplished by the same system. By using immersion oil in combination with a microscope objective having a high $NA = 1.25$, we achieve a small optical excitation volume. The excitation/detection path from underneath the sample requires a fully transparent sample stack with the functionality of a multi-terminal electronic device. We have accomplished this by using commercially available glass substrates coated with ITO that allow for patterning by e-beam lithography and standard micro-/nanofabrication techniques (see 5.1) [100]. CNTs are assembled from solution by an evaporation-driven method reported in Ref. [88]. Figure 5.1b schematically shows a CNT array device having split top gates, similar to previously fabricated layouts [84]. By applying appropriate voltages on each of the two split-gate electrodes it is possible to generate p- and n-doped spatial domains and to create a potential drop across the CNT array. An alternative approach for making a CNT array junction device is depicted in Fig. 5.1c. The layout is based on the fact that the energy band alignment at the CNT/metal contact can be tuned by the work function of the contact metal itself. As a result, a built-in electric field is created inside the device without applying an external bias [93]. In the present case, we use aluminum and palladium as contact metals to induce the built-in electric field across the CNT array. The Fermi level of aluminum aligns closer to the conduction band of CNTs while that of palladium aligns with the valence band of CNTs [89, 101]. Ideally, we expect a device with small Schottky-barriers [93, 101] with a built-in electric field that scales with the work function difference of the contact metals and inversely with the device channel length.

5.2 OPTICAL RESOLUTION

Figure 5.2 shows optical microscopy images of such a device having alternating contacts made of Al and Pd, respectively, positioned along an aligned CNT array. The images were taken by raster scanning a $15x15\mu m^2$ device area with a step size of 50nm with respect to a tightly focused laser beam having a wavelength of $\lambda_{Laser} = 632.8$nm. The polarization of the laser is adjusted parallel to the long axis of the CNTs in the array (i.e. perpendicular to the metal contacts). Apparently, the elastic scattering images and the photocurrent images of the same device area reveal higher contrast and show significant improvement of optical resolution if measured by using the oil immersion. The optical resolution of short-circuit photocurrent images is determined based on the vertical cross sections along two positions for each experimental condition (indicated by arrows in Fig. 5.2a,b) and allows for straightforward comparison of identical features in the photocurrent signal. The spatial extension of photocurrent features in x-direction results from the horizontal alignment of the CNTs in the array, perpendicular to the contacts (see Fig. 5.1c).

We quantify the spatial resolution of our photocurrent measurements by fitting features taken from the photocurrent cross sections with a Gaussian function and extract the full-width-at-half-maximum (FWHM) feature size. We obtain a spatial resolution of $\Delta x_{im} = (250 \pm 40)$nm as compared to $\Delta x = (500 \pm 60)$nm for the same feature if measured without immersion. Based on the density of $50\text{CNT}/\mu$m as derived from the electron microscopy images, we conclude that about 15 CNTs are simultaneously illuminated by the laser focus. Hence, the features observed in the photocurrent images can not be unambiguously attributed to single CNTs. However, the heterogeneous electrostatic potential profile revealed in Fig. 5.2b is not expected by looking at scanning electron microscopy images of the device shown in Fig. 5.1c, despite the much higher spatial resolution. From the scanning

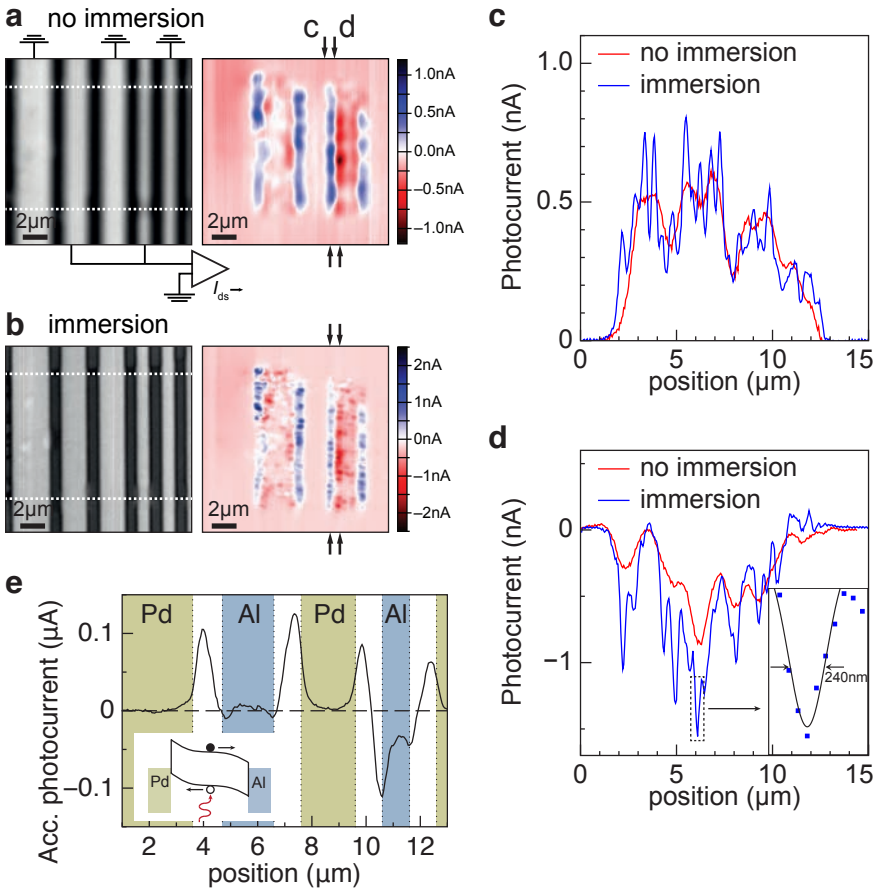

Figure 5.2: Laser scanning microscopy images ($\lambda_{Laser} = 632.8$nm) of the elastically scattered light (left) and short-circuit photocurrent (right) measured (a) without immersion and (b) with immersion. The circuitry for measuring the photocurrent across multiple contact pairs simultaneously is also indicated. (c),(d) Comparison of the photocurrent amplitudes taken from vertical cross sections indicated by arrows in (a) and (b). (e) Accumulated photocurrent amplitudes based on the data shown in (b); the inset illustrates schematically the band profile, exciton generation, and carrier separation. Also indicated are the positions of the contact electrodes (yellow: Pd, blue: Al).

electron microscope images it appears that the CNT array is rather homogeneous with a constant CNT density across the device. In the following, we investigate the usefulness of the method for CNT array device inspection.

5.3 CNTS ARRAY DIODES WITH ASYMMETRIC CONTACTS

In Figure 5.2e we plot the accumulated photocurrent amplitude measured across five alternating contacts having varying contact widths. Accumulation of the photocurrent is performed along the vertical (y-) direction based on the data shown in Fig. 5.2b. Three important observations can be made in this graph. Firstly, the photocurrent amplitude maximum occurs close the center between two adjacent contacts, as could be expected from the energy band alignment according to the work function difference of the metals involved [94]. In one case, however, the photocurrent microscopy reveals a polarity inversion which leads to a reduction of the net photocurrent amplitude generated between the two contacts. The internal, local potential heterogeneity can affect the overall device performance and cannot be observed by analyzing the SEM images of the same device (see Fig. 5.1c). The observation that the spatial maximum of the photocurrent amplitude can be offset or even switch polarity can be attributed to the influence of local environmental doping [102, 103] and to the fact that there are CNTs that do not fully bridge the channel between two contacts, i.e. percolation [104]. The latter is conceivable as the average CNT length of $L_{CNT} = 0.8\mu$m in the array is slightly shorter than the contact separation of $L_{ch} = 1\mu$m.

Secondly, we observe a non-vanishing positive photocurrent signal underneath the Pd contact and a negative one underneath the Al contact, revealing the different interface potentials of CNT-Pd and CNT-Al contacts. This observation was not possible in previous studies because CNT-metal contacts were illuminated from the top. Thirdly, we observe non-vanishing photocurrent amplitude along the entire contact width W if $W \leq 1\mu$m, indicating incomplete carrier transmission at CNT-metal contacts with smaller width. From these observations we can deduce design rules for photovoltaic devices: In order to maximize the net photocurrent generated in a device that is completely

exposed to light, or, in other words, globally illuminated, one would choose to maximize either a positive or a negative photocurrent amplitude. In the present case, in order to maximize the net positive photocurrent in the multi-contact device, one would reduce the channel length between adjacent contacts below the average CNT length, i.e. $L_{ch} < L_{CNT}$. The width of the photocurrent maxima between the contacts is about 500nm (FWHM) and defines the lower limit of L_{ch}. As a result, the efficiency of photocurrent generation is maximized and the impact of CNT-CNT percolation effects is minimized. Based on the CNT density, laser power, and size of the excitation spot we estimate a responsivity per CNT of 0.01nA/μW. Furthermore, one would choose Pd contact widths of $W_{Pd} < 1\mu$m and Al contact widths of $W_{Al} > 1\mu$m. In other words one would reduce the contact width below (or keep it larger) than about $2L_T$ to maximize (minimize) the photocurrent contribution under the corresponding contact. As a result, the maximum of the photocurrent amplitude occurs in the center between adjacent contacts and vanishes underneath the contacts. In the following we investigate in more detail the electrostatic potential and photocurrent generation at the CNT-metal contacts.

Figure 5.3 shows a study of a Pd-CNT-Al device. Fig. 5.3a schematically indicates the device layout and measurement scheme while the measured current-voltage characteristics of three devices having different channel lengths are shown in Fig. 5.3b. The transport measurements demonstrate that the degree of electrical current asymmetry that characterizes diode behavior is inversely proportional to the channel length L_{ch}. For a given metal work function difference $\Delta\phi = \phi_{Pd} - \phi_{Al} \approx 1$eV [101] as in the present case a decrease of channel length L_{ch} increases the local built-in field associated with the electrostatic potential drop. In order to investigate the spatial distribution of the electrostatic potential profile in the device, we analyze the photocurrent in the device channel and underneath the contacts. By comparing the laser scattering image with the corresponding photocurrent image, it is possible to determine the position of the metal

contacts in the photocurrent image with high precision (see Fig. 5.3c). As an important result, the photocurrent amplitude does not vanish abruptly at the contact edges, but clearly extends within the contacts, albeit having different polarities. In Fig. 5.3d we plot cross sections taken from the photocurrent measured underneath the Pd contact (along the red vertical line) and the Al contact (along the blue vertical line). Pronounced photocurrent features are visible in the cross sections that originate from single CNTs or small CNT bundles as can be seen by following the photocurrent traces underneath the metal contacts in Fig. 5.3c. The CNT features are more pronounced at the CNT-Pd interface, suggesting a weaker electrostatic potential drop at the CNT-Al interface. Consequently, one could argue that the Pd-CNT interface has a higher transmission probably for charge carriers and hence get absorbed into the contact over a shorter characteristic length scale.

In general, the measured short-circuit photocurrent is caused by local electric fields that result from bending of energy bands in CNTs. The measured photocurrent is proportional to the local potential gradient, $I_{PC} \propto -d\phi(x)/dx$, where x denotes the position along the device channel and $\phi(x)$ is the potential energy of the electronic band [105, 106]. In order to determine the potential or energy band profile from the short-circuit photocurrent, we numerically integrate the measured photocurrent and the result is shown in Fig. 5.3e. While the maximum photocurrent amplitude is observed close to the Pd contact edge, the maximum of the electrostatic potential is located in the channel center.

The decay of the photocurrent signal within the contact is expected to be exponential for a semiconductor/metal interface and the characteristic decay length L_T of the contact potential $\phi(x) = \phi_0 \exp(-x/L_T)$ is referred to as the charge carrier transfer length [91, 107]. In the present case, characterizes the length scale of charge carriers transit between the CNTs and the metal contact and hence determines the CNT-metal contact resistance . The measured photocurrent signal is

proportional to the potential gradient and we can write which allows us to extract L_T-values by fitting exponential model functions to the measured photocurrent amplitude. In Fig. 5.3f we plot the fits of the normalized, accumulated photocurrent amplitude measured underneath the Pd (red) and Al (blue) contact. We obtain values of $L_T = (240 \pm 18)$nm for the Pd contact and $L_T = (470 \pm 52)$nm for the Al contact. The L_T-values constitute a lower bound for the respective contact width in order to avoid incomplete carrier transmission. They represent an average over roughly 400 CNTs with an average diameter of $d = 1.5$nm and are therefore representative for the specific metal-CNT interface. Our result for the Pd-CNT contact is in agreement with L_T-values of single CNTs derived from electrical transport measurements [108] and similar to the L_T-value of the Pd-graphene interface [63].

5.4 CNTS ARRAY DIODES WITH LOCAL GATES

Finally, we investigate the possibility of controlling the electrostatic potential profile of CNT array devices through local metal gates. A schematic of sample layout and bias scheme is shown in Fig. 5.4a. In order to initially create a symmetric potential profile across the device, Pd was chosen as contact metal for both source and drain electrodes. Two split top gate electrodes define p- or n-doped spatial domains in the covered device areas through application of suitable voltage pairs (V_{tg1}, V_{tg2}). Fig. 5.4b shows a series of short-circuit photocurrent images that were acquired for five different (V_{tg1}, V_{tg2})-combinations. Comparison with the elastically scattered optical signal allows for correlating the measured photocurrent signal with the positions of contacts and gate electrodes. Despite Schottky barriers at the CNT-metal contacts, we do not expect any built-in fields in the device at zero gate bias. Indeed, for $V_{tg1} = V_{tg2} = 0$V a non-vanishing photocurrent response is only observed at the position of the contact edges.

In contrast, by applying either $V_{tg1} = -V_{tg2} = -5\text{V}$ or $V_{tg1} = -V_{tg2} = 5\text{V}$, the maximum (minimum) photocurrent is observed in the intrinsic area of the CNT array framed by the p- and n-doped spatial domains, at the device center. In Fig. 5.4c, we plot the normalized, accumulated photocurrent amplitudes for three representative gate voltage combinations (V_{tg1}, V_{tg2}), overlaid with the elastic scattering signal that indicates the position of contacts and gate electrodes. Based on the accumulated photocurrent, we are able to reveal the electrostatic potential profile of the device through numerical integration (see Fig. 5.4d). The initially flat (in the region between the local gates) and symmetric potential can be tuned such that a potential drop occurs in the region between the split gates with a slope that is determined by the local gate fields applied. As a result, the electrostatic potential in CNT arrays can be fully controlled through field doping by local gates.

Finally, we address contributions from the Schottky barriers at the contacts to the potential profile in the case of strong local gating ($V_{tg1} = -V_{tg2} = -5\text{V}$ or $V_{tg1} = -V_{tg2} = 5\text{V}$). In Fig. 5.4d we find that the potential value at the intersection of the electrostatic potential profiles under strong local gating (red and blue line) is higher than the value at the contacts. This observation suggests that there is an additive potential component originating from the Schottky barriers at the contacts (black line) that shifts the potential profile upwards.

5.5 CONCLUSION

In summary, we have studied the electrostatic potential and the photocurrent generation in optically transparent CNT array devices by using laser-excited photocurrent microscopy with a spatial resolution of 250nm and we have imaged for the bottomside of CNT-metal contacts in functioning optoelectronic devices. We have provided experimental evidence that the work function difference of Pd and Al as

contact metals generates local built-in fields across a CNT array with maximum photocurrent generation efficiency in the channel center, not at the contacts, of the device. We have directly measured a charge carrier transfer lengths of $L_T = (240 \pm 18)$nm for the CNT-Pd contact and $L_T = (470 \pm 52)$nm at the CNT-Al contact. Based on our experimental results, we have devised a strategy for improving the photovoltaic performance of multi-electrode CNT array devices with alternating contact metals. Furthermore, we have demonstrated the control of the location and the polarity of photocurrent in a CNT array by means of electrostatic field doping through local metal gates. Our results provide novel insights into CNT device physics and are important for future optimization of optoelectronic devices based on CNT arrays.

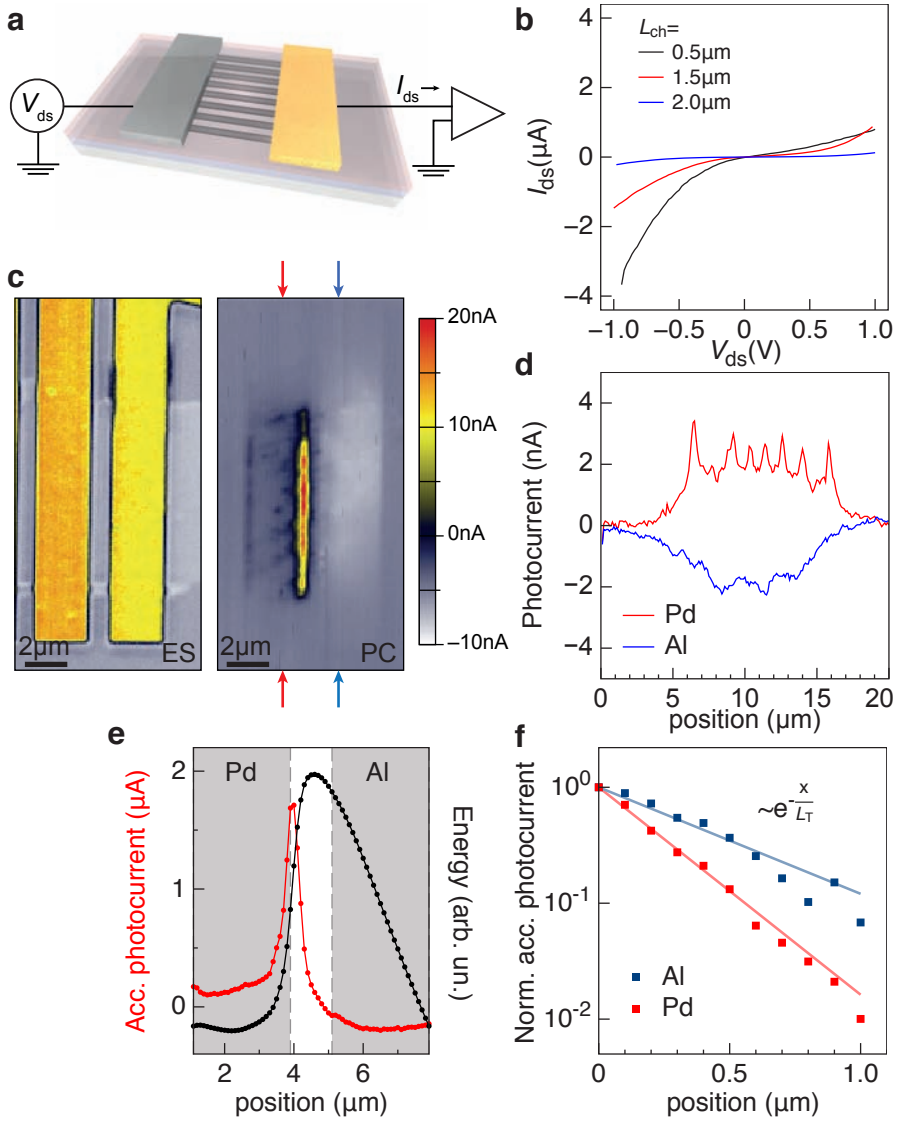

Figure 5.3: (a) 3D visualization of a Pd-CNT-Al array junction device. (b) Measured current-voltage characteristics of three devices having different channel lengths L_{ch}. (c) Microscope images of elastic light scattering (left) and short-circuit photocurrent (right) measured on the same device. (d) Photocurrent amplitudes measured at the bottomside of the Pd-CNT contact (red) and the Al-CNT contact (blue) along the direction indicated by the blue, red vertical lines in (c). (e) Accumulated photocurrent amplitudes (red) along the device and the associated energy band profile (black) obtained by numerical integration of the measured photocurrent signal. (f) Semi-log plot of the normalized accumulated photocurrent amplitude underneath the Pd contact (red) and Al contact (blue). Exponential fits (solid lines) deliver the values of the charge carrier transfer length L_T at the respective CNT-metal contact.

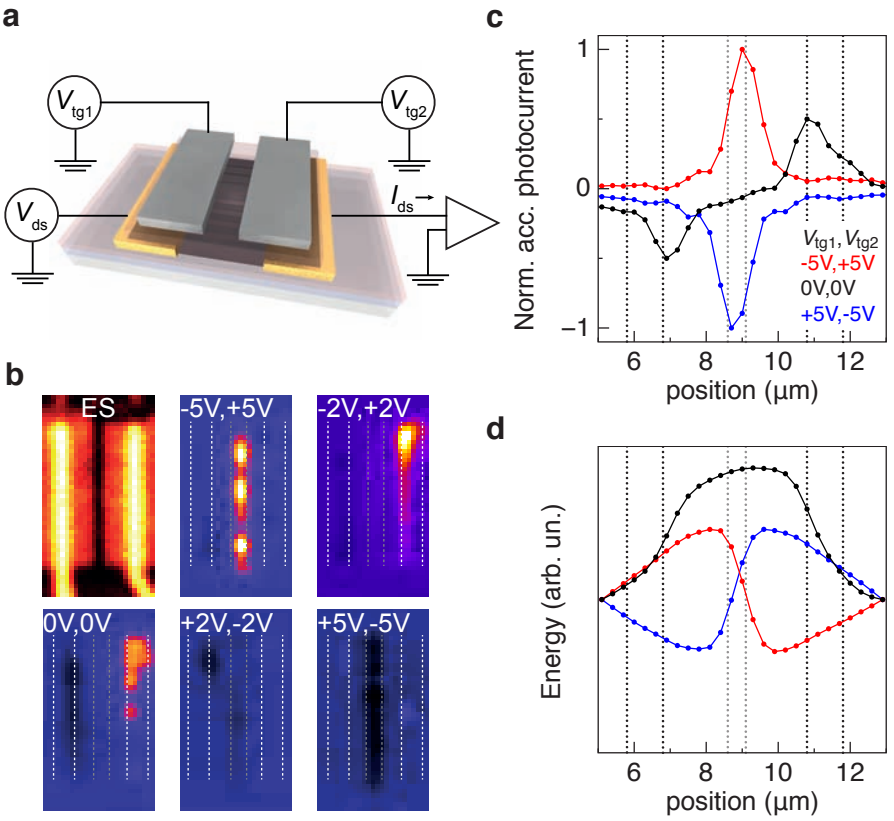

Figure 5.4: (a) 3D visualization of a CNT array device with symmetric contact metals and split top gates. (b) Top left shows the measured signal of elastically scattered light by a split gate device illuminated from the bottomside. The sequence of short-circuit photocurrent images was acquired for the different combinations of top gate voltages (V_{tg1}, V_{tg2}) as indicated; the image size is set to $7.5x13.5\mu m^2$. (c) Normalized accumulated photocurrent based on the data shown in (b) for (V_{tg1}, V_{tg2}) set to $(-5V, +5V)$, $(0V, 0V)$, and $(+5V, -5V)$, respectively. Also indicated are the positions of the contacts and local gates. (d) Electrostatic potential profile obtained by numerical integration of the experimental, accumulated photocurrent amplitudes shown in (c).

BIBLIOGRAPHY

[1] Feynman, R. P. (1988) *QED: The Strange Theory of Light and Matter*. Princeton University Press.

[2] Park, H.-G., Barrelet, C. J., Wu, Y., Tian, B., Qian, F., and Lieber, C. M. (2008) A wavelength-selective photonic-crystal waveguide coupled to a nanowire light source. *Nature Photonics*, **2**, 622–626.

[3] Xia, F., Steiner, M., Lin, Y.-M., and Avouris, P. (2008) A microcavity-controlled, current-driven, on-chip nanotube emitter at infrared wavelengths. *Nature Nanotechnology*, **3**, 609–613.

[4] Gaufrès, E., Izard, N., Le Roux, X., Kazaoui, S., Marris-Morini, D., Cassan, E., and Vivien, L. (2010) Optical microcavity with semiconducting single-wall carbon nanotubes. *Optics Express*, **18**, 5740–5745.

[5] Mueller, T., Xia, F., and Avouris, P. (2010) Graphene photodetectors for high-speed optical communications. *Nature Photonics*, **4**, 297–301.

[6] Furchi, M., et al. (2011) Microcavity-integrated graphene photodetector. *arXiv.org*, **cond-mat.mes-hall**.

[7] Xia, F., Mueller, T., Lin, Y.-M., Valdes-Garcia, A., and Avouris, P. (2009) Ultrafast graphene photodetector. *Nature Nanotechnology*, **4**, 839–843.

[8] Novoselov, K., Geim, A., Morozov, S., Jiang, D., Zhang, Y., Dubonos, S., Grigorieva, I., and Firsov, A. (2004) Electric field effect in atomically thin carbon films. *Science*, **306**, 666–669.

[9] Novoselov, K. S., Geim, A. K., Morozov, S. V., Jiang, D., Katsnelson, M. I., Grigorieva, I. V., Dubonos, S. V., and Firsov, A. A. (2005) Two-dimensional gas of massless Dirac fermions in graphene. *Nature*, **438**, 197–200.

[10] Boehm, H., Clauss, A., Fischer, G., and Hofmann, U. (1961) Dünnste Kohlenstoff-Folien. *Zeitschrift für Naturforschung*, **17b**, 150–153.

[11] Van Bommel, A., Crombeen, J., and Vantooren, A. (1975) Leed and Auger-Electron Observations of SiC (0001) Surface. *Surface Science*, **48**, 463–472.

[12] Pauling, L. (1960) *The Nature of the Chemical Bond and the Structure of Molecules and Crystals: An Introduction to Modern Structural Chemistry*. Cornell University Press.

[13] Saito, R., Dresselhaus, G., and Dresselhaus, M. S. (2005) *Physical Properties of Carbon Nanotubes*. Imperial College Press.

[14] Geim, A. K. and Novoselov, K. S. (2007) The rise of graphene. *Nature Materials*, **6**, 183–191.

[15] Geim, A. K. (2009) Graphene: Status and Prospects. *Science*, **324**, 1530–1534.

[16] Avouris, P. (2010) Graphene: Electronic and Photonic Properties and Devices. *Nano Letters*, **10**, 4285–4294.

[17] Bonaccorso, F., Sun, Z., Hasan, T., and Ferrari, A. C. (2010) Graphene photonics and optoelectronics. *Nature Photonics*, **4**, 611–622.

[18] Liu, M., Yin, X., Ulin-Avila, E., Geng, B., Zentgraf, T., Ju, L., Wang, F., and Zhang, X. (2011) A graphene-based broadband optical modulator. *Nature*, **474**, 64–67.

[19] Ju, L., et al. (2011) Graphene plasmonics for tunable terahertz metamaterials. *Nature Nanotechnology*, **6**, 630–634.

[20] Echtermeyer, T. J., Britnell, L., Jasnos, P. K., Lombardo, A., Gorbachev, R. V., Grigorenko, A. N., Geim, A. K., Ferrari, A. C., and Novoselov, K. S. (2011) Strong plasmonic enhancement of photovoltage in graphene. *Nature Communications*, **2**, 1–5.

[21] Sun, Z., Hasan, T., Torrisi, F., Popa, D., Privitera, G., Wang, F., Bonaccorso, F., Basko, D. M., and Ferrari, A. C. (2010) Graphene Mode-Locked Ultrafast Laser. *ACS Nano*, **4**, 803–810.

[22] Hong, B. H., Lee, J. Y., Beetz, T., Zhu, Y. M., Kim, P., and Kim, K. S. (2005) Quasi-continuous growth of ultralong carbon nanotube arrays. *Journal of the American Chemical Society*, **127**, 15336–15337.

[23] Jorio, A., Dresselhaus, G., and Dresselhaus, M. (2008) *Carbon nanotubes: advanced topics in the synthesis, structure, properties and applications*. Topics in applied physics, Springer.

[24] Huang, L., Cui, X., White, B., and O'Brien, S. P. (2004) Long and oriented single-walled carbon nanotubes grown by ethanol chemical vapor deposition. *Journal of Physical Chemistry B*, **108**, 16451–16456.

[25] Iijima, S. (1991) Helical microtubulus of graphitic carbon. *Nature*, **354**, 56–58.

[26] Javey, A., Kim, H., Brink, M., Wang, Q., Ural, A., Guo, J., Mcintyre, P., McEuen, P., Lundstrom, M., and Dai, H. (2002) High-kappa dielectrics for advanced carbon-nanotube transistors and logic gates. *Nature Materials*, **1**, 241–246.

[27] Koziol, K., Vilatela, J., Moisala, A., Motta, M., Cunniff, P., Sennett, M., and Windle, A. (2007) High-performance carbon nanotube fiber. *Science*, **318**, 1892–1895.

[28] Sazonova, V., Yaish, Y., Üstünel, H., Roundy, D., Arias, T. A., and Mceuen, P. L. (2004) A tunable carbon nanotube electromechanical oscillator. *Nature*, **431**, 284–287.

[29] Lassagne, B., Tarakanov, Y., Kinaret, J., Garcia-Sanchez, D., and Bachtold, A. (2009) Coupling Mechanics to Charge Transport in Carbon Nanotube Mechanical Resonators. *Science*, **325**, 1107–1110.

[30] Iijima, S. and Ichihashi, T. (1993) Single-shell carbon nanitubes of 1-nm diameter. *Nature*, **363**, 603–605.

[31] Bethune, D. S., Kiang, C. H., Devries, M. S., Gorman, G., Savoy, R., Vazquez, J., and Beyers, R. (1993) Cobalt-catalyzed growth of carbon nanotubes with single-atomic-layer walls. *Nature*, **363**, 605–607.

[32] Avouris, P., Freitag, M., and Perebeinos, V. (2008) Carbon-nanotube photonics and optoelectronics. *Nature Photonics*, **2**, 341–350.

[33] Ashcroft, N. W. and Mermin, N. D. (1976) *Solid State Physics*. Brooks Cole.

[34] Reich, S., Thomsen, C., and Maultzsch, J. (2003) *Carbon Nanotubes: Basic Concepts and Physical Properties*. Wiley-VCH.

[35] Wallace, P. R. (1947) The band theory of graphite. *Physical Review*, **71**, 622–634.

[36] Saito, R., Fujita, M., Dresselhaus, G., and Dresselhaus, M. S. (1992) Electronic structure of graphene tubules based on C_{60}. *Physical Review B*, **46**, 1804.

[37] Hone, J., Batlogg, B., Benes, Z., Johnson, A. T., and Fischer, J. E. (2000) Quantized phonon spectrum of single-wall carbon nanotubes. *Science*, **289**, 1730–1733.

[38] Yang, L., Anantram, M. P., Han, J., and Lu, J. P. (1999) Band-gap change of carbon nanotubes: Effect of small uniaxial and torsional strain. *Physical Review B*, **60**, 13874–13878.

[39] Tans, S. J., Verschueren, A. R. M., and Dekker, C. (1998) Room-temperature transistor based on a single carbon nanotube. *Nature*, **393**, 49–52.

[40] Martel, R., Schmidt, T., Shea, H. R., Hertel, T., and Avouris, P. (1998) Single- and multi-wall carbon nanotube field-effect transistors. *Applied Physics Letters*, **73**, 2447–2449.

[41] Falkovsky, L. A. and Varlamov, A. A. (2007) Space-time dispersion of graphene conductivity. *European Physical Journal B*, **56**, 281–284.

[42] Gusynin, V. P., Sharapov, S. G., and Carbotte, J. P. (2006) Unusual microwave response of dirac quasiparticles in graphene. *Phys. Rev. Lett.*, **96**, 256802.

[43] Nair, R. R., Blake, P., Grigorenko, A. N., Novoselov, K. S., Booth, T. J., Stauber, T., Peres, N. M. R., and Geim, A. K. (2008) Fine structure constant defines visual transparency of graphene. *Science*, **320**, 1308–1308.

[44] Bachilo, S., Strano, M., Kittrell, C., Hauge, R., Smalley, R., and Weisman, R. (2002) Structure-assigned optical spectra of single-walled carbon nanotubes. *Science*, **298**, 2361–2366.

[45] Ando, T. (1997) Excitons in carbon nanotubes. *Journal of the Physical Society of Japan*, **66**, 1066–1073.

[46] Spataru, C. D., Ismail-Beigi, S., Benedict, L. X., and Louie, S. G. (2004) Excitonic effects and optical spectra of single-walled carbon nanotubes. *Physical Review Letters*, **92**, 077402.

[47] Wang, F., Dukovic, G., Brus, L. E., and Heinz, T. F. (2005) The optical resonances in carbon nanotubes arise from excitons. *Science*, **308**, 838–841.

[48] Maultzsch, J., Pomraenke, R., Reich, S., Chang, E., Prezzi, D., Ruini, A., Molinari, E., Strano, M. S., Thomsen, C., and Lienau,

C. (2005) Exciton binding energies in carbon nanotubes from two-photon photoluminescence. *Phys. Rev. B*, **72**, 241402.

[49] Burstein, E. and Weisbuch, C. (1995) *Confined electrons and photons: new physics and applications*. NATO ASI series: Physics, Plenum Press.

[50] Purcell, E. M. (1946) Spontaneous emission probabilities at radio frequencies. *Physical Review*, **69**, 681.

[51] Mak, K. F., Sfeir, M. Y., Wu, Y., Lui, C. H., Misewich, J. A., and Heinz, T. F. (2008) Measurement of the optical conductivity of graphene. *Physical Review Letters*, **101**, 196405.

[52] Freitag, M., Chiu, H.-Y., Steiner, M., Perebeinos, V., and Avouris, P. (2010) Thermal infrared emission from biased graphene. *Nature Nanotechnology*, **5**, 497–501.

[53] Berciaud, S., Han, M. Y., Mak, K. F., Brus, L. E., Kim, P., and Heinz, T. F. (2010) Electron and Optical Phonon Temperatures in Electrically Biased Graphene. *Physical Review Letters*, **104**, 227401.

[54] Fermi, E. (1932) Quantum Theory of Radiation. *Reviews of Modern Physics*, **4**, 87–132.

[55] Vahala, K. (2003) Optical microcavities. *Nature*, **424**, 839–846.

[56] Kleppner, D. (1981) Inhibited Spontaneous Emission. *Physical Review Letters*, **47**, 233–236.

[57] Björk, G., Machida, S., Yamamoto, Y., and Igeta, K. (1991) Modification of spontaneous emission rate in planar dielectric microcavity structures. *Physical Review A*, **44**, 669–681.

[58] Steiner, M., Failla, A. V., Hartschuh, A., Schleifenbaum, F., Stupperich, C., and Meixner, A. J. (2008) Controlling molecular broadband-emission by optical confinement. *New Journal of Physics*, **10**, 123017.

[59] Ando, T., Zheng, Y., and Suzuura, H. (2002) Dynamical Conductivity and Zero-Mode Anomaly in Honeycomb Lattices. *Journal of The Physical Society of Japan*, **71**, 1318–1324.

[60] Keizou, K., Chieko, O., and Hiroshi Inoue, T. (2002) Measurement of the characteristic transverse mode radius of a planar microcavity laser. *Japanese Journal of Applied Physics*, **41**, 7398–7399.

[61] Pockrand, I., Brillante, A., and Möbius, D. (1980) Nonradiative decay of excited molecules near a metal surface. *Chemical Physics Letters*, **69**, 499–504.

[62] Calander, N. (2004) Theory and simulation of surface plasmon-coupled directional emission from fluorophores at planar structures. *Anal. Chem*, **76**, 2168–2173.

[63] Xia, F., Perebeinos, V., Lin, Y.-M., Wu, Y., and Avouris, P. (2011) The origins and limits of metal-graphene junction resistance. *Nature Nanotechnology*, **6**, 179–184.

[64] Wang, X., Tabakman, S. M., and Dai, H. (2008) Atomic Layer Deposition of Metal Oxides on Pristine and Functionalized Graphene. *Journal of the American Chemical Society*, **130**, 8152–8153.

[65] Hecht, E. (2002) *Optics*. Addison-Wesley.

[66] Becker, H., Burns, S., Tessler, N., and Friend, R. (1997) Role of optical properties of metallic mirrors in microcavity structures. *Journal of Applied Physics*, **81**, 2825–2829.

[67] Kim, S., Nah, J., Jo, I., Shahrjerdi, D., Colombo, L., Yao, Z., Tutuc, E., and Banerjee, S. K. (2009) Realization of a high mobility dual-gated graphene field-effect transistor with Al_2O_3 dielectric. *Applied Physics Letters*, **94**, 062107.

[68] Adam, S., Hwang, E. H., Galitski, V. M., and Das Sarma, S. (2007) A self-consistent theory for graphene transport. *Proceedings of the National Academy of Sciences*, **104**, 18392–18397.

[69] Lee, E. J. H., Balasubramanian, K., Weitz, R. T., Burghard, M., and Kern, K. (2008) Contact and edge effects in graphene devices. *Nature Nanotechnology*, **3**, 486–490.

[70] Kim, H., Lim, S. C., and Lee, Y. H. (2011) Size effect of two-dimensional thermal radiation. *Physics Letters A*, **375**, 2661–2664.

[71] Freitag, M., Steiner, M., Martin, Y., Perebeinos, V., Chen, Z., Tsang, J. C., and Avouris, P. (2009) Energy Dissipation in Graphene Field-Effect Transistors. *Nano Letters*, **9**, 1883–1888.

[72] Perebeinos, V. and Avouris, P. (2010) Inelastic scattering and current saturation in graphene. *Physical Review B*, **81**, 195442.

[73] Barreiro, A., Lazzeri, M., Moser, J., Mauri, F., and Bachtold, A. (2009) Transport properties of graphene in the high-current limit. *Physical Review Letters*, **103**, 076601.

[74] Avouris, P., Chen, Z., and Perebeinos, V. (2007) Carbon-based electronics. *Nature Nanotechnology*, **2**, 605–615.

[75] Fujiwara, A., Matsuoka, Y., Suematsu, H., Ogawa, N., Miyano, K., Kataura, H., Maniwa, Y., Suzuki, S., and Achiba, Y. (2001) Photoconductivity in semiconducting single-walled carbon nanotubes. *Japanese Journal of Applied Physics Part 2-Letters*, **40**, L1229–L1231.

[76] Freitag, M., Martin, Y., Misewich, J., Martel, R., and Avouris, P. (2003) Photoconductivity of single carbon nanotubes. *Nano Letters*, **3**, 1067–1071.

[77] Balasubramanian, K., Fan, Y., Burghard, M., Kern, K., Friedrich, M., Wannek, U., and Mews, A. (2004) Photoelectronic transport imaging of individual semiconducting carbon nanotubes. *Applied Physics Letters*, **84**, 2400–2402.

[78] Misewich, J., Martel, R., Avouris, P., Tsang, J., Heinze, S., and Tersoff, J. (2003) Electrically induced optical emission from a carbon nanotube FET. *Science*, **300**, 783–786.

[79] Adam, E., Aguirre, C. M., Marty, L., St-Antoine, B. C., Meunier, F., Desjardins, P., Menard, D., and Martel, R. (2008) Electroluminescence from single-wall carbon nanotube network transistors. *Nano Letters*, **8**, 2351–2355.

[80] Wang, S., et al. (2011) High-Performance Carbon Nanotube Light-Emitting Diodes with Asymmetric Contacts. *Nano Letters*, **11**, 23–29.

[81] Pfeiffer, M. H. P., Stürzl, N., Marquardt, C. W., Engel, M., Dehm, S., Hennrich, F., Kappes, M. M., Lemmer, U., and Krupke, R. (2011) Electroluminescence from chirality-sorted (9,7)-semiconducting carbon nanotube devices. *Optics Express*, **19**, A1184–A1189.

[82] Zhou, X., Zifer, T., Wong, B. M., Krafcik, K. L., Leonard, F., and Vance, A. L. (2009) Color Detection Using Chromophore-Nanotube Hybrid Devices. *Nano Letters*, **9**, 1028–1033.

[83] Rowell, M. W., Topinka, M. A., McGehee, M. D., Prall, H.-J., Dennler, G., Sariciftci, N. S., Hu, L., and Gruner, G. (2006) Organic solar cells with carbon nanotube network electrodes. *Applied Physics Letters*, **88**, 233506.

[84] Lee, J. U., Gipp, P. P., and Heller, C. M. (2004) Carbon nanotube p-n junction diodes. *Applied Physics Letters*, **85**, 145.

[85] Lee, J. U. (2005) Photovoltaic effect in ideal carbon nanotube diodes. *Applied Physics Letters*, **87**, 073101.

[86] Yang, L., Wang, S., Zeng, Q., Zhang, Z., Pei, T., Li, Y., and Peng, L.-M. (2011) Efficient photovoltage multiplication in carbon nanotubes. *Nature Photonics*, **5**, 673–677.

[87] Kang, S. J., Kocabas, C., Ozel, T., Shim, M., Pimparkar, N., Alam, M. A., Rotkin, S. V., and Rogers, J. A. (2007) High-performance electronics using dense, perfectly aligned arrays of single-walled carbon nanotubes. *Nature Nanotechnology*, **2**, 230–236.

[88] Engel, M., Small, J. P., Steiner, M., Freitag, M., Green, A. A., Hersam, M. C., and Avouris, P. (2008) Thin Film Nanotube Transistors Based on Self-Assembled, Aligned, Semiconducting Carbon Nanotube Arrays. *ACS Nano*, **2**, 2445–2452.

[89] Javey, A., Guo, J., Wang, Q., Lundstrom, M. S., and Dai, H. (2003) Ballistic carbon nanotube field-effect transistors. *Nature*, **424**, 654–657.

[90] Zhang, Z., et al. (2007) Doping-free fabrication of carbon nanotube based ballistic CMOS devices and circuits. *Nano Letters*, **7**, 3603–3607.

[91] Leonard, F. and Talin, A. A. (2011) Electrical contacts to one- and two-dimensional nanomaterials. *Nature Nanotechnology*, **6**, 773–783.

[92] Freitag, M., Tsang, J. C., Bol, A. A., Yuan, D., Liu, J., and Avouris, P. (2007) Imaging of the schottky barriers and charge depletion in carbon nanotube transistors. *Nano Letters*, **7**, 2037–2042.

[93] Wang, S., Zhang, Z., Ding, L., Liang, X., Shen, J., Xu, H., Chen, Q., Cul, R., Li, Y., and Peng, L.-M. (2008) A doping-free carbon nanotube CMOS inverter-based bipolar diode and ambipolar transistor. *Advanced Materials*, **20**, 3258–3262.

[94] Chen, C., Lu, Y., Kong, E. S., Zhang, Y., and Lee, S.-T. (2008) Nanowelded carbon-nanotube-based solar microcells. *Small*, **4**, 1313–1318.

[95] Gabor, N. M., Zhong, Z., Bosnick, K., Park, J., and Mceuen, P. L. (2009) Extremely Efficient Multiple Electron-Hole Pair Generation in Carbon Nanotube Photodiodes. *Science*, **325**, 1367–1371.

[96] Mueller, T., Kinoshita, M., Steiner, M., Perebeinos, V., Bol, A. A., Farmer, D. B., and Avouris, P. (2010) Efficient narrow-band light emission from a single carbon nanotube p-n diode. *Nature Nanotechnology*, **5**, 27–31.

[97] Kinoshita, M., Steiner, M., Engel, M., Small, J. P., Green, A. A., Hersam, M. C., Krupke, R., Mendez, E. E., and Avouris, P. (2010) The polarized carbon nanotube thin film LED. *Optics Express*, **18**, 25738–25745.

[98] Arnold, M. S., Green, A. A., Hulvat, J. F., Stupp, S. I., and Hersam, M. C. (2006) Sorting carbon nanotubes by electronic structure using density differentiation. *Nature Nanotechnology*, **1**, 60–65.

[99] Hersam, M. C. (2008) Progress towards monodisperse single-walled carbon nanotubes. *Nature Nanotechnology*, **3**, 387–394.

[100] Dattoli, E. N., Wan, Q., Guo, W., Chen, Y., Pan, X., and Lu, W. (2007) Fully transparent thin-film transistor devices based on SnO2 nanowires. *Nano Letters*, **7**, 2463–2469.

[101] Chen, Z., Appenzeller, J., Knoch, J., Lin, Y.-M., and Avouris, P. (2005) The role of metal-nanotube contact in the performance of carbon nanotube field-effect transistors. *Nano Letters*, **5**, 1497–1502.

[102] Aguirre, C. M., Levesque, P. L., Paillet, M., Lapointe, F., St-Antoine, B. C., Desjardins, P., and Martel, R. (2009) The Role of the Oxygen/Water Redox Couple in Suppressing Electron Conduction in Field-Effect Transistors. *Advanced Materials*, **21**, 3087–3091.

[103] Kim, W., Javey, A., Vermesh, O., Wang, O., Li, Y., and Dai, H. (2003) Hysteresis caused by water molecules in carbon nanotube field-effect transistors. *Nano Letters*, **3**, 193–198.

[104] Hu, L., Hecht, D., and Gruner, G. (2004) Percolation in transparent and conducting carbon nanotube networks. *Nano Letters*, **4**, 2513–2517.

[105] Ahn, Y., Dunning, J., and Park, J. (2005) Scanning Photocurrent Imaging and Electronic Band Studies in Silicon Nanowire Field Effect Transistors. *Nano Letters*, **5**, 1367–1370.

[106] Freitag, M., Tsang, J. C., Bol, A. A., Avouris, P., Yuan, D., and Liu, J. (2007) Scanning photovoltage microscopy of potential modulations in carbon nanotubes. *Applied Physics Letters*, **91**, 031101.

[107] Schroder, D. K. (2006) *Semiconductor material and device characterization*. Wiley-IEEE Press.

[108] Franklin, A. D. and Chen, Z. (2010) Length scaling of carbon nanotube transistors. *Nature Nanotechnology*, **5**, 858–862.